ICES REPORT   11-03

January 2011

Solution of Coupled Acoustic-Elastic Wave Propagation Problems with Anelastic Attenuation Using Automatic

by

P. J. Matuszyk, L. F. Demkowicz, C. Torres-Verdin

The Institute for Computational Engineering and Sciences
The University of Texas at Austin
Austin, Texas 78712

Solution of Coupled Acoustic-Elastic Wave Propagation Problems with Anelastic Attenuation Using Automatic hp-Adaptivity

P. J. Matuszyk[a,b], L. F. Demkowicz[c], C. Torres-Verdin[a]

[a]*Department of Petroleum And Geosystems Engineering, The University of Texas at Austin, TX 78712, USA*
[b]*Department of Applied Computer Science and Modeling, Faculty of Metals Engineering and Industrial Computer Science, AGH – University of Science and Technology, Kraków, Poland*
[c]*Institute for Computational Engineering and Sciences (ICES), The University of Texas at Austin, TX 78712, USA*

Abstract

The paper presents a hp-adaptive Finite Element method for a class of coupled acoustics/anelasticity problems with application to modeling of sonic tools in the borehole environment. A careful verification of the methodology and solutions of non-trivial examples involving fast and slow formations with soft layers are presented.

Keywords: acoustic logging, borehole acoustics, wave propagation, linear elasticity, coupled problems, hp-adaptive finite elements

---

1. Introduction

Motivation. Accurate numerical simulations of borehole sonic tools enhance the understanding of sonic logs in complicated scenarios (logging while drilling, multilayer formations, casings, mud invasions etc.) and help to improve the technology and design of new generations of sonic tools. The simulations fall into the class of coupled problems: borehole fluid is modeled with inviscid acoustics, tool and casing with elasticity, and the models for the formation range from relatively simple isotropic elasticity through anisotropic elasticity and viscoelasticity to various poroelasticity theories.

The presented work is a continuation of [1]. The method of choice is the hp Finite Element (FE) method with a fully automatic hp-adaptivity

based on the two-grid paradigm described in [2, 3]. Speaking mathematically, the *hp* method delivers exponential convergence (error vs. number of degrees-of-freedom, CPU time or memory use), for both regular and irregular solutions. The problem under study encounters many of such irregularities. At junctions of three or more different materials, stresses are singular, material anisotropies and the use of Perfectly Matched Layer (PML) leads to internal and boundaries layers. Foremost, however, the solution "lives" mostly along the borehole/formation in presence of strong interface waves. If left unresolved, these irregularities pollute the solution at points of interest (receivers) and result in completely erroneous numerical solutions.

A common misconception is the claim that infinite stresses are non-physical and, therefore, need not be resolved. Although the simplified models based on various elasticity models do result in non-physical infinite stresses (in reality, the material undergoes a plastic deformation), they capture correctly the energy distribution and provide meaningful models away from the singularities. Leaving the singularities unresolved distorts the energy distribution and produces wrong results away from them. Of course, only a comparison with experiments allows for an ultimate validation of the models and this is exactly the direction in which we are heading. Assessing the validity of the model requires high fidelity discretizations with negligible discretization error and this is where the use of *hp* methods is critical.

The presented contribution focuses on extending the *hp* technology to multiphysics coupled problems. A starting point for the new *hp* code developed in the course of this project, has been a new *hp* framework [4] designed for coupled problems (different physics in different subdomains) and supporting the *hp*-adaptivity for elements forming the exact sequence, i.e. H^1-, $H(\text{curl})$-, $H(\text{div})$- and L^2-conforming elements. In this project, only the classical H^1-conforming elements are used. Extending the *hp* adaptive algorithm to coupled problems requires additional modifications of the algorithm which are discussed in this contribution.

The main goal of this paper is however to demonstrate a maturity of the *hp*-technology in context of non-academic, industrial-strength examples. This includes a careful verification of the code and solution of a number of non-trivial examples non-accessible with other methods.

Mathematics of coupled problems. The subjects of acoustics and elasticity are classical. Discussion on linear problems of elastic structures coupled to fluids in bounded and unbounded domains can be found e.g. in [5]. The subject of

2

interest relates to the category of problems involving a compact perturbation of a continuous linear operator see, *e.g.*, [6]. In [7] and [8], Demkowicz has studied the asymptotic stability of those problems and has shown how it relates to the convergence of the eigenvalues of the discrete problem to those of the continuous problem. A rigorous mathematical analysis for a related class of coupled problems can be found in [9]. The analysis does not include the PML truncation. Numerical analysis of the coupled acoustics/elasticity problem with the PML truncation is an open problem.

Simulations of sonic tools. The numerical modeling of the wave propagation problem in the complex borehole environment has nearly 40-years history. First, the semi-analytical methods were used, where the solution of nonlinear dispersion equations and numerical integration in the complex domain were obtained numerically. Almost all of these models assumed radial symmetry. Such approach was documented in various technical papers but the most comprehensive exposition of this topic can be find in [10, 11, 12].

The finite difference time domain technique (FDTD) is currently the most often used method for numerical simulation of sonic logging measurements. At the beginning, the simple model of the open borehole surrounded by homogenous or horizontally layered formation was developed [13]. The FDTD approach was successfully applied to the monopole acoustic logging in boreholes with washouts and damaged zones [14]. Later on, a 2D-FDTD method for simulation axisymmetric problems with multipole acoustic excitation was presented [15]. In [16] a 2.5-D velocity-stress FDTD algorithm for boreholes penetrating a generally anisotropic formation was presented. A parallel 3D version of FDTD method was developed for borehole wave fields in general anisotropic formations [17]. In [18] a non-splitting PML for 2D axisymmetrical FDTD was used to truncate the computational domain. Recently, FDTD method with PML was applied to analysis of elastic-wave propagation in a deviated fluid-filled borehole in arbitrary anisotropic formation [19].

The examples of application of the FE method to model sonic logging in the boreholes is much less numerous. In here we can indicate [20], [1] and [21].

The content of the paper is as follows. We begin in Section 2 with the formulation of the problem. Section 3 describes shortly the *hp* technology and discusses the necessary modifications and updates for coupled problems. Verification of the technology and the code is discussed in Section 4. Examples of non-trivial simulations are presented in Section 5, and we conclude

with some remarks and future work plans in Section 6.

2. A class of coupled acoustic–elastic problems with anelastic attenuation

2.1. Acoustic waves in fluid — time and frequency formulation

Propagation of acoustic waves in the fluid filling the borehole as well as cracks into the formation, can be described as a perturbation of pressure and velocity around a hydrostatic equilibrium state [22], and thus expressed by two coupled equations (continuity and linear momentum laws):

$$\begin{cases} \dfrac{\partial p}{\partial t} + c_f^2 \rho_f \nabla \cdot \mathbf{v} = 0 \\[2mm] \rho_f \dfrac{\partial \mathbf{v}}{\partial t} + \nabla p = 0 \end{cases} \tag{1}$$

where $p(\mathbf{x}, t)$ is the (perturbation of) pressure, $\mathbf{v}(\mathbf{x}, t)$ denotes the velocity in the fluid, ρ_f is the fluid density and c_f stands for the sound speed in the fluid. The system of equations must be accompanied with appropriate boundary and, in the case of an unbounded domain, radiation conditions. Upon eliminating the velocity, the scalar wave equation is obtained:

$$c_f^2 \triangle p + \frac{\partial^2 p}{\partial t^2} = 0. \tag{2}$$

Applying Fourier transform with respect to the time, we obtain the corresponding coupled problem in the frequency domain:

$$\begin{cases} i\omega \hat{p} + c_f^2 \rho_f \nabla \cdot \hat{\mathbf{v}} = 0 \\[2mm] i\omega \rho_f \hat{\mathbf{v}} + \nabla \hat{p} = 0, \end{cases} \tag{3}$$

where $\hat{p}(\mathbf{x}, \omega)$ and $\hat{\mathbf{v}}(\mathbf{x}, \omega)$ are Fourier transforms of the pressure and fluid velocity respectively, and ω denotes the angular frequency. Combining these equations or calculating directly Fourier transform of equation (2), one obtains the Helmholtz equation:

$$\triangle \hat{p} + k_f^2 \hat{p} = 0 \qquad k_f = \frac{\omega}{c_f}. \tag{4}$$

4

A weak form of the equation (4) is given by:

$$
\begin{cases}
\hat{p} \in \hat{p}_D + Q : \\
\displaystyle\int_{\Omega_A} \left(\nabla \hat{p} \cdot \nabla \hat{q} - k_f^2 \hat{p} \hat{q} \right) \, \mathrm{d}\Omega_A = \int_{\Gamma_{AN}} \hat{q} \mathbf{n}_f \cdot \nabla \hat{p} \, \mathrm{d}\Gamma_{AN} \quad \forall \hat{q} \in Q
\end{cases}
\tag{5}
$$

Here Ω_A is a domain occupied by the fluid, $\partial \Omega_A = \Gamma_A$ denotes its boundary, and $\mathbf{n}_f$ denotes the outward unit normal to boundary Γ_A. Function $\hat{p}_D$ stands for an admissible lift of the Dirichlet data, and Q denotes the space of test functions,

$$
Q = \left\{ \hat{q} \in H^1(\Omega_A) : \hat{q}|_{\Gamma_{AD}} = 0 \right\}.
$$

The Neumann boundary $\Gamma_{AN} \subset \Gamma_A$ is partitioned into two disjoint subsets: boundary Γ_{ex} where acoustic source $\mathbf{n} \cdot \nabla \hat{p} = g_{ex}$ is defined, and interface Γ_{AE} with the solid where coupling conditions between fluid and solid are prescribed. Interaction with a truncated part of the domain extending to infinity, is modeled with a PML layer (see Section 2.6) terminated with a homogeneous Dirichlet boundary condition on the remaining part of the boundary: $\Gamma_{AD} = \Gamma_A - \Gamma_{AN}$.

2.2. Waves propagation in elastic solids – time and frequency formulation

Elastic wave propagation in the formation, the tool, and the casing, in the absence of body forces, can be described by the following equations, to be satisfied in elastic domain Ω_E:

$$
\begin{cases}
-\nabla \cdot \boldsymbol{\sigma} + \rho_s \dfrac{\partial^2 \mathbf{u}}{\partial t^2} = 0 \\
\boldsymbol{\sigma} = \mathbf{C} : \boldsymbol{\varepsilon} \\
\boldsymbol{\varepsilon}(\mathbf{u}) = \dfrac{1}{2} \left(\nabla \mathbf{u} + \nabla^T \mathbf{u} \right),
\end{cases}
\tag{6}
$$

Here $\boldsymbol{\sigma}$ stands for the stress tensor, $\boldsymbol{\varepsilon}$ is the strain tensor, $\mathbf{u}$ denotes the displacement vector, ρ_s is the solid density, and $\mathbf{C}$ denotes the elastic ($C_{ijkl} \in \mathbb{R}$) 4-th order compliance tensor. The equations must be accompanied with appropriate boundary and, in the case of an unbounded domain, radiation conditions. For the linear isotropic solid, the tensor $\mathbf{C}$ simplifies to:

$$
C_{ijkl} = \mu(\delta_{ik}\delta_{jl} + \delta_{il}\delta_{jk}) + \lambda \delta_{ij}\delta_{kl},
$$

where λ and μ denote (real) Lamé coefficients. The Lamé coefficients can be defined through characteristic wave speeds in the solid, namely: P-wave speed v_p, and S-wave speed v_s,

$$\mu = \rho_s v_s^2 \qquad \lambda = \rho_s(v_p^2 - 2v_s^2). \tag{7}$$

Applying Fourier transform in time, we obtain the corresponding equations in the frequency domain:

$$\begin{cases} -\nabla \cdot \hat{\boldsymbol{\sigma}} - \rho_s \omega^2 \hat{\mathbf{u}} = 0 \\ \qquad\qquad \hat{\boldsymbol{\sigma}} = \mathbf{C} : \hat{\varepsilon} \\ \qquad \hat{\varepsilon}(\hat{\mathbf{u}}) = \dfrac{1}{2}\left(\nabla\hat{\mathbf{u}} + \nabla^T \hat{\mathbf{u}}\right), \end{cases} \tag{8}$$

where $\hat{\boldsymbol{\sigma}}$, $\hat{\varepsilon}$, and $\hat{\mathbf{u}}$ denote the Fourier transforms of the appropriate quantities.

The equations are equipped with two kinds of boundary conditions: homogeneous displacement (Dirichlet) BC imposed on part of the boundary $\Gamma_{ED} \subset \Gamma_E$, $\Gamma_E = \partial\Omega_E$, and (Neumann) tractions BC $\mathbf{n}_s \cdot \hat{\boldsymbol{\sigma}} = \mathbf{t}$ prescribed on the remaining part of the boundary $\Gamma_{EN} = \Gamma_E - \Gamma_{ED}$. Here $\mathbf{n}_s$ stands for the outward unit normal to boundary Γ_E.

A weak form of the equation (8) is given by:

$$\begin{cases} \hat{\mathbf{u}} \in \hat{\mathbf{u}}_D + \mathbf{W} : \\ \displaystyle\int_{\Omega_E}\left(\hat{\varepsilon}_{\hat{\mathbf{w}}} : \mathbf{C} : \hat{\varepsilon}_{\hat{\mathbf{u}}} - \rho_s\omega^2\hat{\mathbf{u}}\cdot\hat{\mathbf{w}}\right)\, \mathrm{d}\Omega_E = \int_{\Gamma_{EN}} \mathbf{t}\cdot\hat{\mathbf{w}}\,\mathrm{d}\Gamma_{EN} \quad \forall \hat{\mathbf{w}} \in \mathbf{W} \end{cases} \tag{9}$$

where $\hat{\mathbf{u}}_D$ is an admissible lift of the Dirichlet data, and $\mathbf{W}$ is the space of test functions defined by:

$$\mathbf{W} = \left\{\hat{\mathbf{w}} \in \mathbf{H}^1(\Omega_E) : \hat{\mathbf{w}}|_{\Gamma_{ED}} = 0\right\}.$$

The Neumann boundary Γ_{EN} is then divided into two disjoint parts: Γ_{EA} where coupling conditions between solid and fluid are prescribed, and the remaining part on which zero traction is prescribed. Similarly to the acoustic case, the interaction with an unbounded part extending to infinity is truncated with a PML layer (see Section 2.6) terminated with homogeneous Dirichlet boundary conditions.

2.3. Coupling conditions between fluid and solid

Coupling conditions at the interface between fluid and solid assure the compatibility of displacements, i.e. the equality of the normal component of velocities:

$$\mathbf{n}_f \cdot \hat{\mathbf{v}} = \mathbf{n}_f \cdot (i\omega\hat{\mathbf{u}}),$$

and tractions:

$$\mathbf{t} = \mathbf{n}_s \cdot \hat{\boldsymbol{\sigma}} = -\mathbf{n}_s \hat{p}.$$

Using equation (3_2), the first condition can be expressed as:

$$\mathbf{n}_f \cdot \nabla\hat{p} = \rho_f \omega^2 \mathbf{n}_f \cdot \hat{\mathbf{u}}.$$

Thus, finally, the weak form for the coupled acoustic-elastic problem is given by:

$$
\begin{cases}
(\hat{\mathbf{u}}, \hat{p}) \in (\hat{\mathbf{u}}_D, \hat{p}_D) + \mathbf{W} \times Q : \\
b_{AA}(\hat{p}, \hat{q}) + b_{AE}(\hat{\mathbf{u}}, \hat{q}) = l_A(\hat{q}) \quad \forall \hat{q} \in Q, \\
b_{EA}(\hat{p}, \hat{\mathbf{w}}) + b_{EE}(\hat{\mathbf{u}}, \hat{\mathbf{w}}) = 0 \quad \forall \hat{\mathbf{w}} \in \mathbf{W},
\end{cases}
$$

where:

$$b_{AA}(\hat{p}, \hat{q}) = \int_{\Omega_A} \left(\nabla\hat{p} \cdot \nabla\hat{q} - k_f^2 \hat{p}\hat{q} \right) \, \mathrm{d}\Omega_A$$

$$b_{AE}(\hat{\mathbf{u}}, \hat{q}) = -\int_{\Gamma_{AE}} \rho_f \omega^2 \hat{q} \mathbf{n}_f \cdot \hat{\mathbf{u}} \, \mathrm{d}\Gamma_{AE}$$

$$b_{EA}(\hat{p}, \hat{\mathbf{w}}) = \int_{\Gamma_{EA}} \hat{p}\mathbf{n}_s \cdot \hat{\mathbf{w}} \, \mathrm{d}\Gamma_{EA}$$

$$b_{EE}(\hat{\mathbf{u}}, \hat{\mathbf{w}}) = \int_{\Omega_E} \left(\hat{\boldsymbol{\varepsilon}}_{\hat{\mathbf{w}}} : \mathbf{C} : \hat{\boldsymbol{\varepsilon}}_{\hat{\mathbf{u}}} - \rho_s \omega^2 \hat{\mathbf{u}} \cdot \hat{\mathbf{w}} \right) \, \mathrm{d}\Omega_E$$

$$l_A(\hat{q}) = \int_{\Gamma_{ex}} \hat{q} g_{ex} \, \mathrm{d}\Gamma_{ex}$$

2.4. Modeling anelastic attenuation

It is observed fact that energy of the elastic waves in the formation exhibits some damping due to internal friction, presence of fluids and a non-homogeneous structure of the formation (grains, crystal imperfections, fractures, etc) [10]. The attenuation is frequency dependent and has stronger

effects for higher frequencies causing a decrease of the wave amplitude and change of wave velocity. Several methods have been developed to deal with the attenuation [23]. One of the classical approaches describing this phenomenon is based on the theory of viscoelasticity which complements the classical elastic theory strain with velocity dependent terms. Consequently, the stress does not depend solely on the strain but also takes into account the strain history. Another approach used to model the attenuation phenomenon is "an analysis based on the constraints imposed by causality on wave propagation". We follow the second method and use constant-Q model [24].

We define the complex wavenumbers, complex wave velocities and complex compliance tensor to modify the classical elastic equations. Lame coefficients are defined by characteristic wave velocities in the solid (equations 7). Additional parameters describing attenuation in the model are so called quality factors Q_p and Q_s which express the damping rate in one wave cycle. In the presented model, one assumes that these factors are frequency independent. The method defines the complex phase velocity:

$$ c(\omega) = c_0 \left(1 + \frac{1}{\pi Q} \ln \frac{\omega}{\omega_0} \right) \left(1 + \frac{i}{2Q} \right), \qquad (10) $$

where c_0 is a reference velocity at angular frequency ω_0. The authors suggest to use a reference frequency $1Hz$ [24], that corresponds to angular frequency $\omega_0 = 2\pi$. The equation above is often replaced with a simpler version, neglecting the term with factor $1/Q^2$. The same approach can be used to model attenuation in a fluid which for the presented problem can represent water or oil base mud, hydrocarbon or brine present in the formation cracks. The increase of seismic velocities with frequency agrees with experiments over the range of frequencies from $100Hz$–$100kHz$ [11].

Having given pairs (v_p^0, Q_p) and (v_s^0, Q_s) and setting $\omega_0 = 2\pi$, one can calculate complex phase velocities:

$$ v_p = v_p^0 \left(1 + \frac{1}{\pi Q_p} \ln f \right) \left(1 + \frac{i}{2Q_p} \right), $$

$$ v_s = v_s^0 \left(1 + \frac{1}{\pi Q_s} \ln f \right) \left(1 + \frac{i}{2Q_s} \right), $$

where v_p^0 and v_s^0 are low frequency limit reference velocities, and f denotes the frequency.

Thus, accounting for the attenuation in the wave propagation problem, one simply has to replace characteristic wave velocities with the complex velocities, resulting in the corresponding complex and frequency dependent acoustic wavenumber k_f, and solid compliance tensor C.

2.5. Modeling of multipole acoustic sources

Almost all logging tools are based on a combination of monopole, dipole or quadrupole acoustic sources. A proper numerical model for such sources is needed.

A monopole source can be modeled with an acoustic point source which exhibits spherical symmetry pattern of the radiation. Multipole sources of order n can be constructed from the collection of $2n$ monopole point sources placed periodically in the same plane, along a circle of radius r_0, alternating in sign [25]. Furthermore, such a model of the multipole source can be

Monopole   Dipole   Quadrupole
$n = 0$ $n = 1$ $n = 2$
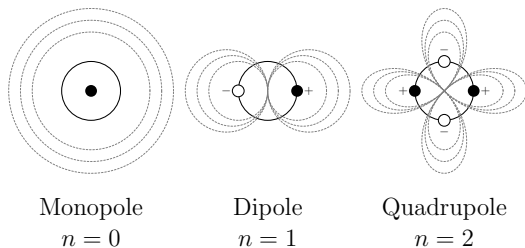
Figure 1: Models for multipole acoustic sources

approximated with a Fourier expansion in the azimuthal direction θ. The monopole source is 0 order, dipole source is of the 1st order and consists of two point sources of opposite sign, an the quadrupole source consists of four monopole sources, located at angles $k\pi/2$. The leading term in the radiation pattern for the n-order multipole source exhibits $\cos(n\theta)$ dependence in azimuthal angle θ (see Fig. 1). Therefore, one can approximate a multipole source of order n by:

$$g_{ex}^{(n)} = p_0 \cos(n\theta) = \underbrace{\frac{p_0}{2} e^{in\theta}}_{g_n^+} + \underbrace{\frac{p_0}{2} e^{-in\theta}}_{g_n^-} \qquad n = 0, 1, 2, \ldots \qquad (11)$$

Use of complex exponentials instead of the cosine function enables a further simplification of the variational formulation of the problem in cylindrical coordinates, and makes possible to decrease the dimension of the calculated

9

problem. Due to the linearity of the problem, solution $(\hat{p}_n, \hat{\mathbf{u}}_n)$ of n-th azimuthal order can be computed as a superposition of solutions $(\hat{p}_n^+, \hat{\mathbf{u}}_n^+)$ and $(\hat{p}_n^-, \hat{\mathbf{u}}_n^-)$ calculated independently for exciting sources g_n^+ and g_n^- respectively.

Assuming an excitation of the form given by g_n^+ we arrive at the following definitions of trial and test functions:

$$
\begin{aligned}
\hat{p}_n^+ &= p_n(r,z)e^{in\theta} & \hat{\mathbf{u}}_n &= \mathbf{u}_n(r,z)e^{in\theta} \\
\hat{q}_n^+ &= q_n(r,z)e^{-in\theta} & \hat{\mathbf{w}}_n &= \mathbf{w}_n(r,z)e^{-in\theta}
\end{aligned}
\tag{12}
$$

where p_n, q_n, $\mathbf{u}_n$ and $\mathbf{w}_n$ are solely functions of r and z coordinates.

Monopole source $(n = 0)$.. The source excites only one mode. Consequently, one can solve the problem with excitation source equal g_n^+, and then multiply the solution by 2. The source pattern is axially symmetric, the solution does not depend upon the azimuthal direction θ and, therefore, can be directly solved for in 2D (r, z) domain. Furthermore, the test and trial functions are of the same form which implies for the presented problems a (complex-valued) symmetric stiffness matrix.

Multipole source $(n > 0)$.. The source excites two modes. In this case, it is still enough to calculate only solution $(\hat{p}_n, \hat{\mathbf{u}}_n)$ for excitation g_n^+, however, the bilinear form is now not symmetric and contains all terms. Due to symmetries and antisymmetries in bilinear forms $b_n^+ \left((\hat{p}^+, \hat{\mathbf{u}}^+), (\hat{q}^+, \hat{\mathbf{w}}^+) \right)$, and $b_n^- \left((\hat{p}^-, \hat{\mathbf{u}}^-), (\hat{q}^-, \hat{\mathbf{w}}^-) \right)$, one can observe that:

$$
\begin{aligned}
b_n^- \left((\hat{p}^-, \hat{u}_r^-, \hat{u}_\theta^-, \hat{u}_z^-), (\hat{q}^-, \hat{w}_r^-, \hat{w}_\theta^-, \hat{w}_z^-) \right) = \\
b_n^+ \left((\hat{p}^+, \hat{u}_r^+, -\hat{u}_\theta^+, \hat{u}_z^+), (\hat{q}^+, \hat{w}_r^+, -\hat{w}_\theta^+, \hat{w}_z^+) \right)
\end{aligned}
$$

and furthermore, the load vectors for both cases are the same, because:

$$
g_n^+ \hat{q}^+ = g_n^- \hat{q}^- = \frac{p_0}{2} q_n(r,z).
$$

Thus, the solution for the problem with excitation g_n^- can be directly calculated from the solution of the problem with excitation g_n^+, which halfs the computational time. Components $\hat{p}$, $\hat{u}_r$, $\hat{u}_\theta$ and $\hat{u}_z$ for constant values of n are solely functions of r and z coordinates enabling thus the solution only in 2D trace (r, z) domain.

The final solution $(\hat{p}_n, \hat{\mathbf{u}}_n)$ is calculated in terms of the solution for one excitation mode only, as follows:

$$\hat{p}_n = \frac{1}{2}\left(\hat{p}^+ e^{in\theta} + \hat{p}^- e^{-in\theta}\right) \qquad = \hat{p}^+ \cos(n\theta) \tag{13}$$

$$\hat{\mathbf{u}}_n = \frac{1}{2}\left(\begin{bmatrix} \hat{u}_r^+ e^{in\theta} \\ \hat{u}_\theta^+ e^{in\theta} \\ \hat{u}_z^+ e^{in\theta} \end{bmatrix} + \begin{bmatrix} \hat{u}_r^- e^{-in\theta} \\ \hat{u}_\theta^- e^{-in\theta} \\ \hat{u}_z^- e^{-in\theta} \end{bmatrix}\right) \qquad = \begin{bmatrix} \hat{u}_r^+ \cos(n\theta) \\ \hat{u}_\theta^+ i\sin(n\theta) \\ \hat{u}_z^+ \cos(n\theta) \end{bmatrix} \tag{14}$$

Transforming the solution into time domain.. Having calculated solutions for sufficiently many frequencies, the inverse Fourier transform [1] is performed delivering the solution in time domain:

$$p(\mathbf{x}, t) = \frac{1}{2\pi}\int_{-\infty}^{\infty} \hat{p}(\mathbf{x}, \omega)e^{i\omega t}\,\mathrm{d}\omega \qquad \approx \frac{\Delta\omega}{2\pi}\sum_{n=-c}^{c} \hat{p}(\mathbf{x}, \omega_n)e^{i\omega_n t} \tag{15}$$

$$\mathbf{u}(\mathbf{x}, t) = \frac{1}{2\pi}\int_{-\infty}^{\infty} \hat{\mathbf{u}}(\mathbf{x}, \omega)e^{i\omega t}\,\mathrm{d}\omega \qquad \approx \frac{\Delta\omega}{2\pi}\sum_{n=-c}^{c} \hat{\mathbf{u}}(\mathbf{x}, \omega_n)e^{i\omega_n t}, \tag{16}$$

where $\Delta\omega$ is a chosen frequency step, c is a number of discrete frequencies used, and $\omega_i = n\Delta\omega$ is a discrete angular frequency. The frequency spacing $\Delta\omega$ should be chosen in such a way that $\Delta\omega < \frac{\pi}{T}$, where $2T$ is an anticipated simulation time.

The number of needed frequencies c depends on the spectrum of excitation and the response. In particular, if the excitation source has a compact/narrow spectrum and that spectrum decays quickly with increasing frequency then one can neglect higher frequencies for which the spectrum is negligibly small.

2.6. Perfectly Matched Layer (PML)

A general problem of wave propagation in a borehole–formation system is posed in an unbounded domain. An effective numerical simulation of this problem using FEM needs a truncated domain, and special techniques are needed for truncating boundary conditions to avoid reflections of outward propagating waves. For this purpose, the PML method was used.

For the problem defined in frequency domain, and cylindrical coordinates (r, θ, z) the PML absorbing layer is constructed by a complex stretching of

---

[1] We use the inverse FFT in actual computations.

the axial (z) and radial (r) coordinates. Given a wavenumber k, we use the following transformation:

$$x_j := X_j(x_j, k) \qquad \frac{\partial}{\partial x_j} := \frac{1}{X_j'}\frac{\partial}{\partial x_j} \qquad \text{where} \qquad X_j' = \frac{\partial X_j}{\partial x_j}. \qquad (17)$$

The transformation of coordinates x_j results in an analytic continuation of the solution into a complex plane characterized with an exponential decay of the outgoing waves, and an exponential blow-up of the incoming waves in the stretched direction (r or z) within the PML absorbing region. Consequently, imposing a homogeneous Dirichlet boundary at the end of the PML region does not affect the ("stretched") outgoing wave but it eliminates the incoming one. It is of a utmost practical importance to construct the stretching in such a way that the attenuated outgoing wave reaches a machine zero on the PML outer boundary.

The general form of the stretching transformation in direction X_j can be written as follows:

$$X_j(x_j, k) = g_j(x_j, k)(1 - i) + x_j \qquad (18)$$
$$X_j'(x_j, k) = g_j'(x_j, k)(1 - i) + 1 \qquad (19)$$
$$X_j''(x_j, k) = g_j''(x_j, k)(1 - i) \qquad (20)$$

where i is an imaginary unit and a function $g_j(x_j, k)$ is defined by:

$$g_j(x_j, k) = \frac{2^p}{k}a(\xi)^m\frac{\xi'}{|\xi'|} \quad \text{where} \quad [0,1] \ni \xi(x_j) = \begin{cases} \frac{x_j^L - x_j}{\delta_j} & x_j < x_j^L \\ \frac{x_j - x_j^R}{\delta_j} & x_j > x_j^R \\ 0 & \text{otherwise.} \end{cases} \qquad (21)$$

The simultaneous stretching of both real and imaginary parts produces an effect that not only the plain waves but also evanescent waves are damped within the PML region. Computational domain in x_j-direction is contained in $[x_j^L - \delta_j, x_j^R + \delta_j]$, $x_j^L < x_j^R$, where δ_j is the PML width in x_j-direction. Function a maps $[0,1]$ onto itself. Parameter p controls the strength of the wave attenuation. For instance, it can be estimated as

$$p \geqslant \frac{\ln(d\ln 10)}{\ln 2}$$

if we want to decrease amplitude of the incident wave by factor 10^d. For $p = 5$, the wave amplitude attenuation on the outer boundary of the PML is

Name	a
(ver-1)	ξ
(ver-2)	$\xi - \frac{\sin 2\pi\xi}{2\pi}$
(Bramble-Pasciak)[26]	$\xi^3[10 - \xi(15 - 6\xi)]$

Table 1: Proposed choices of auxiliary stretching functions a.

of order 10^{-14}, and for $p = 6$ the amplitude decrease is of order 10^{-28}, which – assuming wave amplitudes of order 1 into the simulated domain – gives values below the machine zero on a standard computer.

The last step in definition of stretching function g is the definition of auxiliary function $a : [0, 1] \rightarrow [0, 1]$ such that $a(0) = 0$ and $a(1) = 1$. The term a^m controls the way in which the attenuation of the wave is increased as we go deeper into the absorbing layer. Some choices of the function a are presented in Table (1).

2.7. Formulation in cylindrical coordinates

The cylindrical coordinates, due to the axial symmetry of the geometry of the problem, as well as due to convenient approach for the representation of multipole nonsymmetric sources (presented in the previous sections), are a natural choice for the presented problem.

Formulation for acoustics.. First, one has to define gradients of the functions $\hat{p}$ and $\hat{q}$ under PML stretching and using function definitions (12):

$$\nabla\hat{p} = \left[\frac{\partial\hat{p}}{\partial r}, \frac{1}{r}\frac{\partial\hat{p}}{\partial\theta}, \frac{\partial\hat{p}}{\partial z}\right] \xrightarrow{PML, (12)} \left[\frac{1}{R'}\frac{\partial\hat{p}_n}{\partial r}, \frac{+in\hat{p}_n}{R}, \frac{1}{Z'}\frac{\partial\hat{p}_n}{\partial z}\right] e^{in\theta}$$

$$\nabla\hat{q} = \left[\frac{\partial\hat{q}}{\partial r}, \frac{1}{r}\frac{\partial\hat{q}}{\partial\theta}, \frac{\partial\hat{q}}{\partial z}\right] \xrightarrow{PML, (12)} \left[\frac{1}{R'}\frac{\partial\hat{q}_n}{\partial r}, \frac{-in\hat{q}_n}{R}, \frac{1}{Z'}\frac{\partial\hat{q}_n}{\partial z}\right] e^{-in\theta}$$

Now, taking into account that the jacobian $\mathrm{d}\Omega_A = r\,\mathrm{d}r\,\mathrm{d}\theta\,\mathrm{d}z$ is transformed, due to the PML stretching, into $\mathrm{d}\Omega_A = RR'Z'\,\mathrm{d}r\,\mathrm{d}\theta\,\mathrm{d}z$, one arrives at the final weak form for acoustic equation:

$$\int_{\Omega_A} \left(\frac{RZ'}{R'}\right)\frac{\partial\hat{p}_n}{\partial r}\frac{\partial\hat{q}_n}{\partial r} + \left(\frac{RR'}{Z'}\right)\frac{\partial\hat{p}_n}{\partial z}\frac{\partial\hat{q}_n}{\partial z} + \left(n^2\frac{R'Z'}{R} - k_f^2 RR'Z'\right)\hat{p}_n\hat{q}_n\,\mathrm{d}\Omega_A$$

$$- \rho_f\omega^2 \int_{\Gamma_{AE}} \hat{q}_n\mathbf{n}_f\cdot\hat{\mathbf{u}}\,RR'Z'\,\mathrm{d}\Gamma_{AE} = \int_{\Gamma_{ex}} \hat{q}_n\frac{p_0}{2}RR'Z'\,\mathrm{d}\Gamma_{ex} \quad \forall\hat{q}_n \in Q. \quad (22)$$

13

The corresponding energy space is defined as a weighted H^1 space:

$$Q = \left\{ q : \left| \frac{RZ'}{R'} \right|^{\frac{1}{2}} \frac{\partial q}{\partial r}, \left| \frac{RR'}{Z'} \right|^{\frac{1}{2}} \frac{\partial q}{\partial z}, n \left| \frac{R'Z'}{R} \right|^{\frac{1}{2}} q, |RR'Z'|^{\frac{1}{2}} q \in L_2(\Omega_A), q|_{\Gamma_{AD}} = 0 \right\}$$

Formulation for elasticity.. In here, one has to first define strain tensor components expressed in cylindrical coordinates:

$$\varepsilon_{rr} = \frac{\partial u_r}{\partial r} \qquad\qquad \varepsilon_{rz} = \frac{1}{2} \left(\frac{\partial u_r}{\partial z} + \frac{\partial u_z}{\partial r} \right)$$

$$\varepsilon_{zz} = \frac{\partial u_z}{\partial z} \qquad\qquad \varepsilon_{r\theta} = \frac{1}{2} \left[\frac{\partial u_\theta}{\partial r} - \frac{1}{r} \left(u_\theta - \frac{\partial u_r}{\partial \theta} \right) \right]$$

$$\varepsilon_{\theta\theta} = \frac{1}{r} \left(\frac{\partial u_\theta}{\partial \theta} + u_r \right) \qquad\qquad \varepsilon_{\theta z} = \frac{1}{2} \left(\frac{\partial u_\theta}{\partial z} + \frac{1}{r} \frac{\partial u_z}{\partial \theta} \right)$$

perform an analogous PML stretching, and introduce function definitions (12):

$$\varepsilon_{rr}(\hat{\mathbf{u}}) = \alpha \frac{1}{R'} \frac{\partial \hat{u}_r}{\partial r} \qquad\qquad \varepsilon_{rr}(\hat{\mathbf{w}}) = \beta \frac{1}{R'} \frac{\partial \hat{w}_r}{\partial r}$$

$$\varepsilon_{zz}(\hat{\mathbf{u}}) = \alpha \frac{1}{Z'} \frac{\partial \hat{u}_z}{\partial z} \qquad\qquad \varepsilon_{zz}(\hat{\mathbf{w}}) = \beta \frac{1}{Z'} \frac{\partial \hat{w}_z}{\partial z}$$

$$\varepsilon_{\theta\theta}(\hat{\mathbf{u}}) = \alpha \frac{1}{R} (\hat{u}_r + in\hat{u}_\theta) \qquad\qquad \varepsilon_{\theta\theta}(\hat{\mathbf{w}}) = \beta \frac{1}{R} (\hat{w}_r - in\hat{w}_\theta)$$

$$\varepsilon_{rz}(\hat{\mathbf{u}}) = \alpha \frac{1}{2} \left(\frac{1}{Z'} \frac{\partial \hat{u}_r}{\partial z} + \frac{1}{R'} \frac{\partial \hat{u}_z}{\partial r} \right) \qquad \varepsilon_{rz}(\hat{\mathbf{w}}) = \beta \frac{1}{2} \left(\frac{1}{Z'} \frac{\partial \hat{w}_r}{\partial z} + \frac{1}{R'} \frac{\partial \hat{w}_z}{\partial r} \right)$$

$$\varepsilon_{r\theta}(\hat{\mathbf{u}}) = \alpha \frac{1}{2} \left(\frac{1}{R'} \frac{\partial \hat{u}_\theta}{\partial r} - \frac{\hat{u}_\theta - in\hat{u}_r}{R} \right) \qquad \varepsilon_{r\theta}(\hat{\mathbf{w}}) = \beta \frac{1}{2} \left(\frac{1}{R'} \frac{\partial \hat{w}_\theta}{\partial r} - \frac{\hat{w}_\theta + in\hat{w}_r}{R} \right)$$

$$\varepsilon_{\theta z}(\hat{\mathbf{u}}) = \alpha \frac{1}{2} \left(\frac{1}{Z'} \frac{\partial \hat{u}_\theta}{\partial z} + \frac{in\hat{u}_z}{R} \right) \qquad\quad \varepsilon_{\theta z}(\hat{\mathbf{w}}) = \beta \frac{1}{2} \left(\frac{1}{Z'} \frac{\partial \hat{w}_\theta}{\partial z} - \frac{in\hat{w}_z}{R} \right)$$

where we have dropped subscript n for displacement components, $\alpha = e^{in\theta}$ and $\beta = e^{-in\theta} = 1/\alpha$. Thus, for the most general considered case we have:

$$\hat{\boldsymbol{\varepsilon}}_{\hat{\mathbf{w}}} : \mathbf{C} : \hat{\boldsymbol{\varepsilon}}_{\hat{\mathbf{u}}} = (2\mu + \lambda) \left[\varepsilon_{rr}(\hat{\mathbf{u}})\varepsilon_{rr}(\hat{\mathbf{w}}) + \varepsilon_{\theta\theta}(\hat{\mathbf{u}})\varepsilon_{\theta\theta}(\hat{\mathbf{w}}) + \varepsilon_{zz}(\hat{\mathbf{u}})\varepsilon_{zz}(\hat{\mathbf{w}}) \right] \quad (23)$$
$$+ \lambda \left[\varepsilon_{rr}(\hat{\mathbf{u}})\varepsilon_{\theta\theta}(\hat{\mathbf{w}}) + \varepsilon_{\theta\theta}(\hat{\mathbf{u}})\varepsilon_{rr}(\hat{\mathbf{w}}) + \varepsilon_{rr}(\hat{\mathbf{u}})\varepsilon_{zz}(\hat{\mathbf{w}}) \right]$$
$$+ \lambda \left[\varepsilon_{zz}(\hat{\mathbf{u}})\varepsilon_{rr}(\hat{\mathbf{w}}) + \varepsilon_{\theta\theta}(\hat{\mathbf{u}})\varepsilon_{zz}(\hat{\mathbf{w}}) + \varepsilon_{zz}(\hat{\mathbf{u}})\varepsilon_{\theta\theta}(\hat{\mathbf{w}}) \right]$$
$$+ 4\mu \left[\varepsilon_{r\theta}(\hat{\mathbf{u}})\varepsilon_{r\theta}(\hat{\mathbf{w}}) + \varepsilon_{rz}(\hat{\mathbf{u}})\varepsilon_{rz}(\hat{\mathbf{w}}) + \varepsilon_{\theta z}(\hat{\mathbf{u}})\varepsilon_{\theta z}(\hat{\mathbf{w}}) \right]$$

and the final equation for elasticity is obtained from the second equation (9) replacing $\hat{\boldsymbol{\varepsilon}}_{\hat{\mathbf{w}}} : \mathbf{C} : \hat{\boldsymbol{\varepsilon}}_{\hat{\mathbf{u}}}$ term according to definition (23), and taking into account stretching jacobian factor $RR'Z'$ in each integral.

In the case of a monopole source ($n = 0$, fully axisymmetric problem), the bilinear form decouples into two independent bilinear forms, where the first depends only on r and z components and the second on θ component only. Similar decomposition follows for the load vector. Assuming that $\hat{\mathbf{u}}_\theta = 0$, solution reduces to determining the $\hat{\mathbf{u}}_r$ and $\hat{\mathbf{u}}_z$ components only, and the final bilinear and linear forms simplify to r and z dependent counterparts.

The energy space for the PML formulation is defined analogously to the acoustic case as a weighted $\mathbf{H}^1$ space.

2.8. Alternative choice of unknowns

Looking at the integrals contributing to the energy norm (22,23), we arrive at the problem of securing additional conditions assuring finiteness of the energy at the axis of symmetry ($r = 0$).

Let us consider first the monopole case. The acoustic bilinear form contains no singular terms but the elastic bilinear form for elasticity includes a singular term $\varepsilon_{\theta\theta} = \hat{u}_r/r$. Two possible scenarios can occur. If the elastic material is placed off of the axis of symmetry (open borehole or logging–while–drilling (LWD) tools), there is no singularity in the elastic energy functional. However simulation of a wireline (solid) tool leads to the presence of the singular term in the elastic energy.

Two solutions are presented to overcome this problem. In the first (we call this approach "formulation A" hereafter), no conditions are prescribed on the axis of symmetry in the elastic domain. Consequently, for all elements adjacent to the axis of symmetry, no additional boundary integrals are computed. As the volume integrals are computed using standard (non-adaptive) Gauss quadrature, integration of the singular term results effectively in an implicit penalty term which forces the radial displacement component u_r to vanish on the axis of symmetry.

A similar situation occurs for the multipole sources ($n > 0$). In here however, there are more singular terms in the energy norms, in acoustics we have the term p^2/r^2, and in elasticity we have term $\varepsilon_{\theta z} \sim u_z/r$, as well as terms $\varepsilon_{\theta\theta}$ and $\varepsilon_{r\theta}$ which are proportional to linear combinations of $(u_r + iu_\theta)/r$. Therefore, for each possible geometry of the problem, the presented phenomenon exists.

Another approach, which we call the "formulation B" deals with the problem through a proper choice of alternative independent variables. For monopole sources, we consider new variables $\hat{u}'_r$, $\hat{u}'_z$, $\hat{p}'$ defined as:

$$\hat{u}_r = r\hat{u}'_r \qquad \hat{u}_z = \hat{u}'_z \qquad \hat{p} = \hat{p}'.$$

Therefore, now the term $\varepsilon_{\theta\theta}$ is proportional to $\hat{u}'_r$, and it is automatically equal zero for $r = 0$ which in turn makes the elastic energy finite. The stretched strain tensor for monopole source has the following components:

$$\varepsilon_{rr}(\hat{\mathbf{u}}') = \alpha\frac{1}{R'}\left(\hat{u}'_r + r\frac{\partial \hat{u}'_r}{\partial r}\right) \qquad \varepsilon_{rr}(\hat{\mathbf{w}}') = \beta\frac{1}{R'}\left(\hat{w}'_r + r\frac{\partial \hat{w}'_r}{\partial r}\right)$$

$$\varepsilon_{zz}(\hat{\mathbf{u}}') = \alpha\frac{1}{Z'}\frac{\partial \hat{u}'_z}{\partial z} \qquad \varepsilon_{zz}(\hat{\mathbf{w}}') = \beta\frac{1}{Z'}\frac{\partial \hat{w}'_z}{\partial z}$$

$$\varepsilon_{\theta\theta}(\hat{\mathbf{u}}') = \alpha\frac{r\hat{u}'_r}{R} \qquad \varepsilon_{\theta\theta}(\hat{\mathbf{w}}') = \beta\frac{r\hat{w}'_r}{R}$$

$$\varepsilon_{rz}(\hat{\mathbf{u}}') = \alpha\frac{1}{2}\left(\frac{r}{Z'}\frac{\partial \hat{u}'_r}{\partial z} + \frac{1}{R'}\frac{\partial \hat{u}'_z}{\partial r}\right) \quad \varepsilon_{rz}(\hat{\mathbf{w}}') = \beta\frac{1}{2}\left(\frac{r}{Z'}\frac{\partial \hat{w}'_r}{\partial z} + \frac{1}{R'}\frac{\partial \hat{w}'_z}{\partial r}\right)$$

"Formulation B" for a multipole source is obtained through the following choice of the independent variables:

$$\hat{u}_r = \hat{u}'_r \qquad \hat{u}_z = r\hat{u}'_z \qquad \hat{u}_\theta = \hat{u}'_\theta \qquad \hat{p} = \hat{p}'.$$

Therefore acoustic energy and the $\varepsilon_{\theta z}$ are finite at the axis of symmetry. We are still left with singular terms $\varepsilon_{\theta\theta}$ and $\varepsilon_{r\theta}$. The ansatz to enforce an automatic vanishing of the quantity $(u_r + iu_\theta)/r$ at $r = 0$ requires considering vector-valued shape functions for elasticity and it is much more difficult to implement. The stretched strain tensor for monopole source has the following components:

$$\varepsilon_{rr}(\hat{\mathbf{u}}') = \alpha\frac{1}{R'}\frac{\partial \hat{u}'_r}{\partial r} \qquad \varepsilon_{rr}(\hat{\mathbf{w}}') = \beta\frac{1}{R'}\frac{\partial \hat{w}'_r}{\partial r}$$

$$\varepsilon_{zz}(\hat{\mathbf{u}}') = \alpha\frac{r}{Z'}\frac{\partial \hat{u}'_z}{\partial z} \qquad \varepsilon_{zz}(\hat{\mathbf{w}}') = \beta\frac{r}{Z'}\frac{\partial \hat{w}'_z}{\partial z}$$

$$\varepsilon_{\theta\theta}(\hat{\mathbf{u}}') = \alpha\frac{1}{R}\left(\hat{u}'_r + in\hat{u}'_\theta\right) \qquad \varepsilon_{\theta\theta}(\hat{\mathbf{w}}') = \beta\frac{1}{R}\left(\hat{w}'_r - in\hat{w}'_\theta\right)$$

$$\varepsilon_{rz}(\hat{\mathbf{u}}') = \frac{\alpha}{2}\left(\frac{1}{Z'}\frac{\partial \hat{u}'_r}{\partial z} + \frac{r}{R'}\frac{\partial \hat{u}'_z}{\partial r} + \frac{\hat{u}'_z}{R'}\right) \quad \varepsilon_{rz}(\hat{\mathbf{w}}') = \frac{\beta}{2}\left(\frac{1}{Z'}\frac{\partial \hat{w}'_r}{\partial z} + \frac{r}{R'}\frac{\partial \hat{w}'_z}{\partial r} + \frac{\hat{w}'_z}{R'}\right)$$

16

$$\varepsilon_{r\theta}(\hat{\mathbf{u}}') = \alpha \frac{1}{2} \left[\frac{1}{R'} \frac{\partial \hat{u}'_\theta}{\partial r} - \frac{\hat{u}'_\theta - in\hat{u}'_r}{R} \right] \qquad \varepsilon_{r\theta}(\hat{\mathbf{w}}') = \beta \frac{1}{2} \left[\frac{1}{R'} \frac{\partial \hat{w}'_\theta}{\partial r} - \frac{\hat{w}'_\theta + in\hat{w}'_r}{R} \right]$$

$$\varepsilon_{\theta z}(\hat{\mathbf{u}}') = \alpha \frac{1}{2} \left(\frac{1}{Z'} \frac{\partial \hat{u}'_\theta}{\partial z} + \frac{inr\hat{u}'_z}{R} \right) \qquad \varepsilon_{\theta z}(\hat{\mathbf{w}}') = \beta \frac{1}{2} \left(\frac{1}{Z'} \frac{\partial \hat{w}'_\theta}{\partial z} - \frac{inr\hat{w}'_z}{R} \right)$$

3. *hp* Technology

3.1. *A new hp-FE code for multiphysics problems*

The presented work has been implemented within a new version of our 2D *hp* code for coupled, multiphysics problems [4]. The principal characteristics on the new code include:

- support of discretizations using a simultaneous use of all elements forming the exact sequence: H^1-, $H(\mathrm{curl})$-, $H(\mathrm{div})$-, and L^2-conforming elements [2],

- support of (weakly) coupled problems,

- energy driven automatic *hp*-adaptivity [2, 3]

In particular, the discussed project led to a non-trivial modification of the automatic *hp*-adaptivity algorithm for a coupled problem (different systems of equations in different parts of the domain) discussed below.

3.2. *Modification of hp algorithm for coupled multiphysics problems through automatic norm scaling*

The *hp*-algorithm two-grid paradigm is based on calculating local energy norms on element edges and in element interiors. In the presented case we deal with two different media, solid and fluid, and thus different physical phenomena and different quantities for which we solve the system of equations – elastic displacements and acoustic pressure. The energy norms corresponding to the two problems have dramatically different values, even if a standard non-dimensionalization is used. In the examples to follow, the energy norm in the acoustical domain was typically larger than the one in the elastic domain, by several orders of magnitude. This implies that the resolution of the elastic part of the domain becomes of a secondary importance. Large differences in energy lead also to possible conditioning problems, even if a direct

---

[2] Only H^1-conforming elements are used in this project.

solver is used. This can be observed e.g. by monitoring pivots reported by the solver.

Therefore, a key-point to a successful application of the automatic hp adaptivity to the coupled problem is to rescale the governing equations to balance quantitatively the acoustic and elastic energy norms. Once the equations are rescaled in such a way that energy norms for a current hp step are equal then the comparison of relative errors in both domains will be meaningful and thus fully justified.

Let $\hat{\mathbf{u}} = s_u \tilde{\mathbf{u}}$ and $\hat{p} = s_p \tilde{p}$. This implies the following scaling for linear and bilinear forms:

$$
\begin{cases}
\dfrac{s_p}{s_u} b_{AA}(\tilde{p}, \hat{q}) + b_{AE}(\tilde{\mathbf{u}}, \hat{q}) = \dfrac{1}{s_u} l_A(\hat{q}) & \forall \hat{q} \in Q, \\[2ex]
b_{EA}(\tilde{p}, \hat{\mathbf{w}}) + \dfrac{s_u}{s_p} b_{EE}(\tilde{\mathbf{u}}, \hat{\mathbf{w}}) = 0 & \forall \hat{\mathbf{w}} \in \mathbf{W},
\end{cases}
$$

and the corresponding scaling for the norms:

$$
|\!|\!|\hat{p}|\!|\!|_A = s_p |\!|\!|\tilde{p}|\!|\!|_A \qquad |\!|\!|\hat{\mathbf{u}}|\!|\!|_E = s_u |\!|\!|\tilde{\mathbf{u}}|\!|\!|_E.
$$

Now, if we set $s_p = |\!|\!|\hat{p}|\!|\!|_A$ and $s_u = |\!|\!|\hat{\mathbf{u}}|\!|\!|_E$, then the energy norms of the scaled solutions $|\!|\!|\tilde{p}|\!|\!|_A$ and $|\!|\!|\tilde{\mathbf{u}}|\!|\!|_E$ be of order 1. Consequently, that enables to compare relative errors of both solutions.

The modified automatic hp algorithm has now the form:

1. set $s_p = s_u = 1$,
2. solve the problem for $(\tilde{\mathbf{u}}, \tilde{p})$
3. save new values $s'_p = |\!|\!|\hat{p}|\!|\!|_A$ and $s'_u = |\!|\!|\hat{\mathbf{u}}|\!|\!|_E$
4. FOR each hp step DO
   (a) set $s_p \leftarrow s'_p$, $s_u \leftarrow s'_u$,
   (b) perform classical hp-step, calc new solution $(\tilde{\mathbf{u}}, \tilde{p})$,
   (c) save new values $s'_p = s_p |\!|\!|\hat{p}|\!|\!|_A$ and $s'_u = s_u |\!|\!|\hat{\mathbf{u}}|\!|\!|_E$

4. Verification of the code

Before we continue with several practical examples, we would like to present necessary steps we have taken to verify the code and justify the choice of several parameters like the frequency range or PML parameters. The verification process has been carried out in several steps, starting with decoupled acoustic and elastic problems for which analytical solutions exist,

and continuing then with the coupled problem and comparisons with other software.

The ultimate results are produced in the time-domain through the application of the inverse Fourier transform integrated numerically, and the first technical decisions concerned the necessary frequency range for the simulations.

4.1. Acoustic source model

The most frequently used model for a sonic source in borehole simulations is the Ricker wavelet, see Fig. 2, due to its fast decay in both time and frequency domains [24]:

$$p(t) = \frac{2}{\sqrt{\pi}} \left[1 - 2 \left(\frac{t - t_0}{T} \right)^2 \right] e^{-\left(\frac{t - t_0}{T} \right)^2} \tag{24}$$

$$\hat{p}(\omega) = 4Te^{-i\omega t_0} \Omega^2 e^{-\Omega^2} \qquad \Omega = \frac{\omega T}{2} = \pi f T. \tag{25}$$

In the above, t_0 is a time at which maximum of the pulse occurs and $T = \frac{1}{\pi f_c}$ is a characteristic period of the pulse defined by so called central frequency f_c. Given a central frequency f_c, the frequency spectrum of the Ricker wavelet
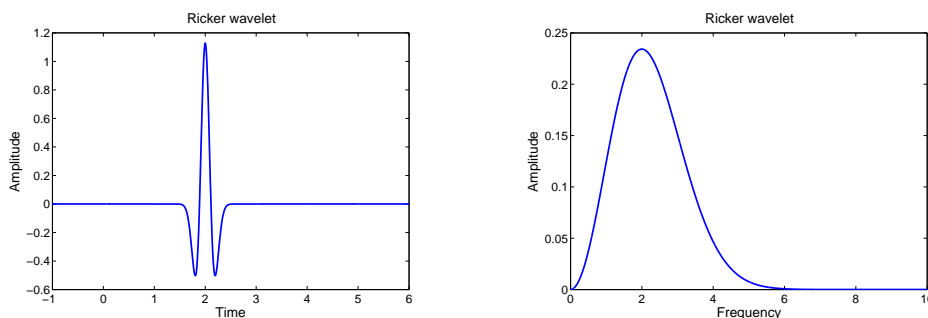
Figure 2: Ricker wavelet: $f_c = 2$, $t_0 = 2$.

is essentially contained between 0 and $3f_c$ which is sufficiently accurate in application to the presented cases. Using this rule, one can easily estimate the required frequency range in typical well-logging applications [12]:

- for a monopole source, we will use central frequency $f_c = 8$ kHz, that gives range $(0, 25)$ kHz; in this case the frequency step equal 50 Hz will be used;

19

- for a dipole and a quadrupole source we will use $f_c = 2$ kHz or $f_c = 3$ kHz, which gives ranges $(0, 6)$ kHz and $(0, 9)$ kHz respectively; for these cases the 25 Hz frequency step will be used.

4.2. Pure acoustic case

For the purpose of verifying the acoustic part of the hp multiphysics code, two different cases were considered: with a point source (Fig. 3(a)) and a ring source (Fig. 3(b)). The fluid density $\rho_f = 1000$ kg/m^3 and sound speed $c_f = 1500$ m/s were used in both cases. In the first case (Fig. 3(a)), the

(a) Point source   (b) Ring source
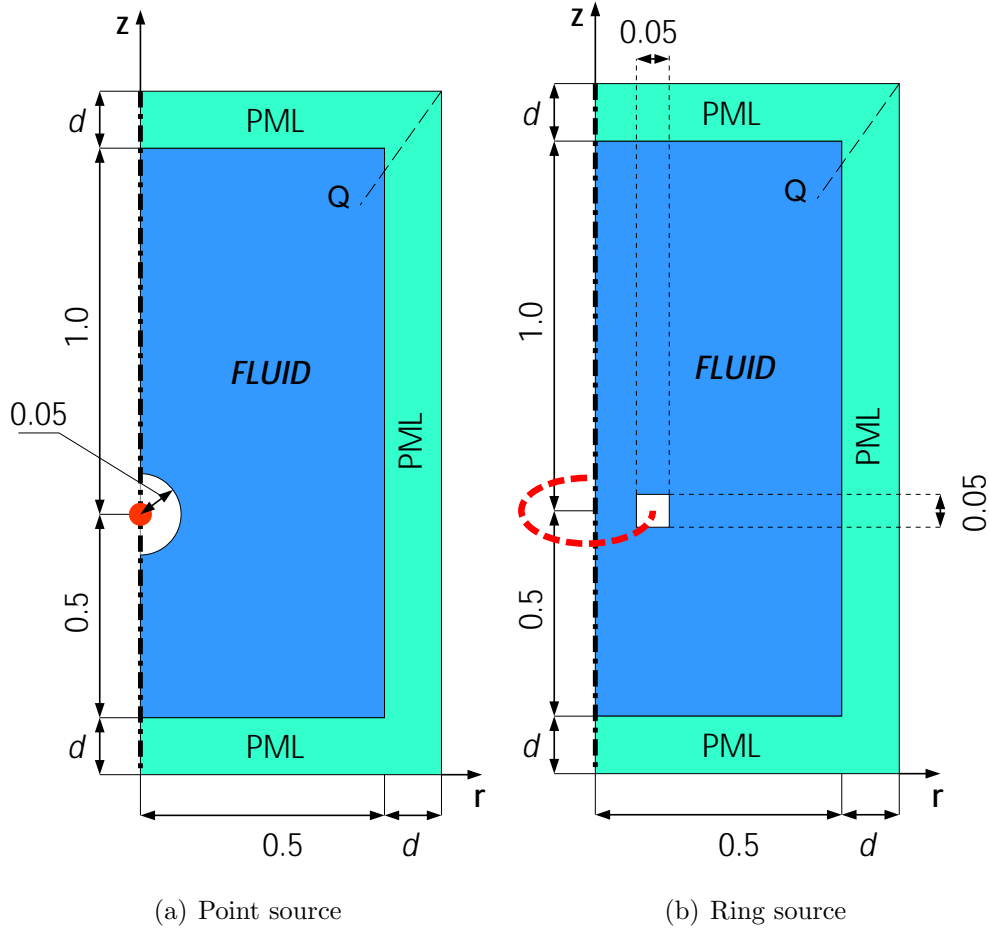
Figure 3: Geometries for the pure acoustic problems.

calculated solution is compared to the analytical solution for the Helmholtz

equation for point monopole and dipole sources. The fluid pressure for a monopole point source in cylindrical coordinates is given by:

$$p^M(r, z) = \frac{1}{4\pi R} e^{-ik_f R} \qquad R = \sqrt{r^2 + z^2}.$$

The field is spherically symmetric.

The dipole acoustic source is realized by placing two monopole sources of opposite sign at $[d, 0, 0]$ and $[d, \pi, 0]$ ($2d$ is the distance between the two monopoles that constitute the acoustic dipole) which results in the pressure pattern that exhibits $\cos\phi$ azimuthal dependence and it is axially symmetric with respect to z-axis. Thus it conforms to the assumptions for multipole sources presented in Section 2.5. The pressure field is given by:

$$p^D(r, z) = -\frac{d}{2\pi R}\left(\frac{1}{R} + ik_f\right) e^{-ik_f R}\frac{r\cos\theta}{R},$$

where θ is the azimuthal angle. In the presented cases, a value $d = 0.01$ m was used.

For both monopole and dipole source, the problem is solved in $[0, 0.5] \times [-0.5, 1]$ m domain with the circular hole of radius 5 cm surrounding the point source cut (see Fig. 3(a)). The source is introduced through the Neumann boundary condition prescribed on the edge of the circular hole.

In the second case (Fig. 3(b)), the ring source is modeled as a superposition of monopole point sources placed around a circle of radius 5 cm, perpendicular to the z-axis. This case is more realistic for the borehole sonic logging and reflects the construction of real monopole sources used in wireline logging tools. The analytical equation describing acoustic field pressure generated by such a source (of 0 thickness) is given by [27]:

$$p(r, z) = \frac{a}{4\pi}\int\limits_0^{2\pi} \frac{e^{-ik_f R}}{R}\,\mathrm{d}\theta \qquad R^2 = r^2 + a^2 - 2ar\cos\theta + z^2,$$

where a is the ring radius and the integration is performed in the azimuthal direction. Here, a numerical integration is needed to calculate the solution and solution derivatives at a point. We used the Romberg's method for that purpose. The source is introduced through the Neumann boundary condition prescribed on the edges of a square hole surrounding the ring source.

(a) Fine mesh

(b) Re(p)

(c) $\log |p_f - p_{ex}|$

(d) Re(p) (red) and $|p|$ (blue) along the profile (zoomed in PML zone, PML marked in blue)
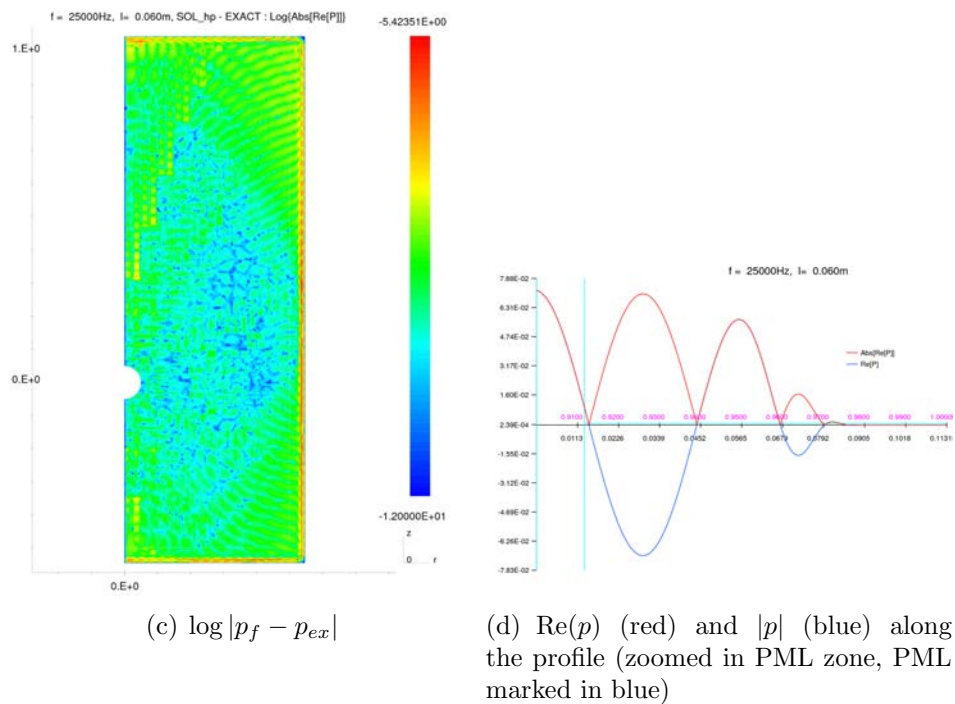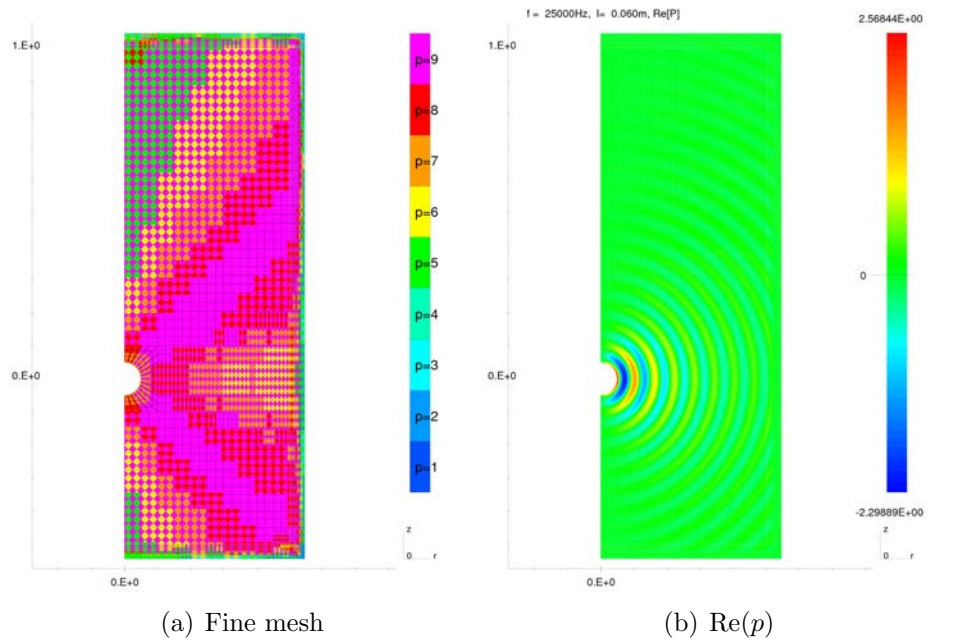
Figure 4: Acoustics. Dipole point source. Formulation A. $f = 25$ kHz

As an example, in Figure 4 we present the results of the simulation for acoustic dipole at frequency 25 kHz. The final *hp*-refined optimal mesh is presented in subfigure (a). Colors are used to indicate the orders of particular edges and element interiors, according to the enclosed scale. One can observe that the mesh refinements conform the solution distribution (presented in subfigure (b)): e.g. solution along *z*-axis for dipole is very small, thus the corresponding elements are relatively large and use lower orders of approximation). Accurate resolution of the large gradients of the solution within the PML results in appropriate mesh refinements close to the PML interface.

In subfigure (c), logarithm of the modulus of the difference between calculated and analytical solution is plotted. This provides an insight on the error distribution over the mesh. For solution magnitude of order 1, the observed error is of order 10^{-7} and less. Higher values of the error are encountered within the PML layer; the PML stretched solution exhibits a strong boundary layer whose resolution is more demanding and results in extensive refinements. Nevertheless, the larger error in the PML region does not seem to affect the error within the domain of interest.

Behavior of the solution within the PML layer is presented in subfigure (d). The solution is plotted along profile Q (see Figure 3 for the definition of the profile). We show here the real part and the modulus of the pressure. The beginning of the PML is indicated by the vertical line; PML continues then to the right. One can observe that the solution is properly damped and attains the machine zero value at 2/3 of the PML depth.

The remaining examples are presented in Appendix Appendix A: with the monopole point source at frequency 50 Hz (Figure A.30) and 25 kHz (Figure A.31), with the monopole ring source at frequency 50 Hz (Figure A.32) and 25 kHz (Figure A.33), with the dipole source at frequency 50 Hz (Figure A.34 for formulation A and Figure A.35 for formulation B) and 25 kHz (Figure A.36 for formulation B).

The PML technique works properly in both low and high frequency regime. The automatically generated mesh refinements for low and high frequency cases, reflect well the fact that the *hp* algorithm aims at minimizing the error in the energy norm. For low frequencies, the solution within the domain of interest changes very slowly (wavelength for the simulated fluid at 50 Hz is 30 m) and is very smooth – large elements with high polynomial order are used. On the other side, the solution within the PML has high gradients and thus high energy error, which in turn produces most of the

refinements in that layer and results in generation of much smaller elements of lower order in the *hp*-refined mesh.

For high frequencies, the energy distribution is more balanced which is reflected in a more uniform distribution of the refinements throughout the mesh. The size of mesh elements is also related to the smallest wavelength (for the simulated fluid at 25 kHz, $\lambda = 6$ cm).

All presented examples show that the self-adaptive *hp* code is able to accurately resolve the acoustic wave propagation problem for multipole sources at the range of frequencies $[50 - 25000]$ Hz. Convergence curves (for point monopole in Figure 5, for ring monopole in Figure 6, for dipole in Figure 7 for formulation A, and in Figure 8 for formulation B, respectively) obtained for all test problems indicate at least an algebraic convergence. In each plot we present three curves corresponding to:

- relative energy error of the coarse solution with respect to the fine mesh (red curve),

- relative energy error of the coarse solution with respect to the analytical solution (black curve), and

- relative error of the fine solution with respect to the analytical solution (blue curve).

We remind the reader that refinements of the coarse grid are driven by the fine grid solution. The kinks present in the convergence curves result from an introduction of new scales in the fine grid solution that successfully enter the picture as the mesh is refined (see [2], Section 15.3 for a related discussion).

4.3. Pure elastic case

For the verification of the elastic part of the *hp* multiphysics code, the case with a source placed at the origin of the coordinate system surrounded by a circular hole was considered (Fig. 3(a)). In all tests, a homogenous fast formation was assumed, described by the following parameters: $\rho_s = 2200$ kg/m^3, $v_p = 3048$ m/s, $v_s = 1793$ m/s, and both quality factors equal ∞ (no anelastic attenuation).

The analytical solutions for displacements excited by a monopole or dipole impulsive source can be developed from the Stokes-Love solution for the
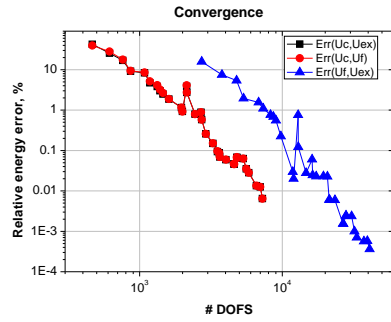
(a) $f = 50$ Hz
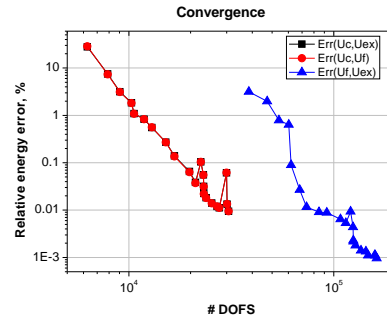
(b) $f = 25$ kHz

Figure 5: Convergence for acoustics. Monopole point source. Formulation A.
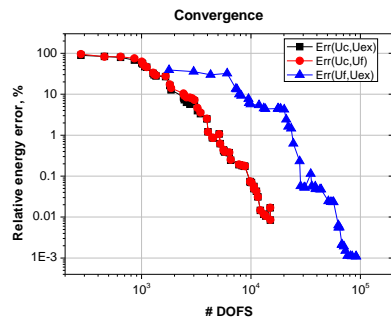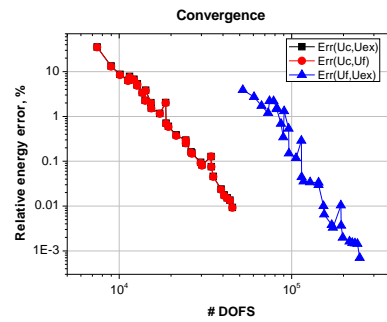
(a) $f = 50$ Hz

(b) $f = 25$ kHz

Figure 6: Convergence for acoustics. Ring source. Formulation A.
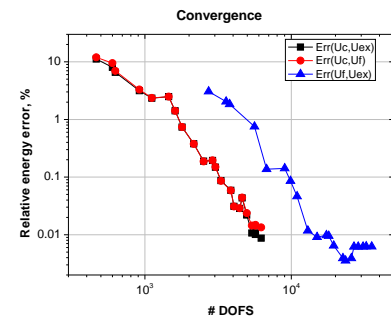
(a) $f = 50$ Hz
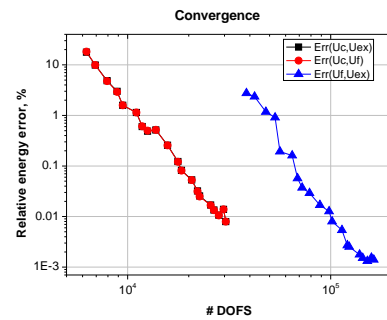
(b) $f = 25$ kHz

Figure 7: Convergence for acoustics. Dipole point source. Formulation A.

25

(a) $f = 50$ Hz
(b) $f = 25$ kHz
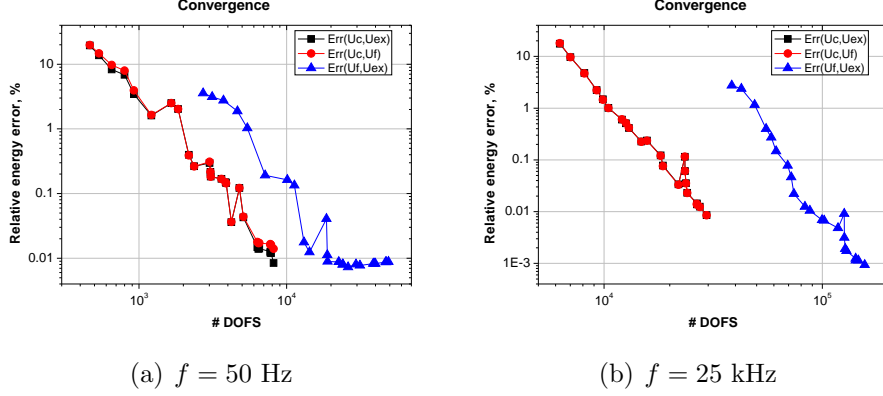
Figure 8: Convergence for acoustics. Dipole point source. Formulation B.

Navier equations given in frequency domain [28]:

$$v_p^2 \nabla \nabla \cdot \mathbf{u} - v_s^2 \nabla \times \nabla \times \mathbf{u} + \omega^2 \mathbf{u} = -\frac{\hat{\mathbf{f}}}{\rho_s},$$

where $\hat{\mathbf{f}}$ is the impulsive source of a force magnitude $\hat{F}_0$, concentrated at the point $\mathbf{r}_0$, acting in direction $\mathbf{a}$ and expressed by:

$$\hat{\mathbf{f}} = \hat{F}_0(\omega)\delta(\mathbf{r} - \mathbf{r}_0)\mathbf{a},$$

where $\mathbf{a}$ is a unit vector, and δ denotes the Dirac distribution. We take $\mathbf{r}_0 = 0$. Solution of the problem in cylindrical coordinates is given by:

$$u_i = \hat{F}_0 \, G_{ij} a_j,$$

where G_{ij} is the Green's dyadic which gives the i-th component of the displacement for force acting along the j-th direction. The Green's diadic in cylindrical coordinates (r, θ, z) is given by:

$$G_{ij}(\mathbf{x}, \mathbf{y}; \omega) = \frac{1}{4\pi\rho\omega^2}
\begin{bmatrix}
k_\beta^2 S + \dfrac{\partial^2 Q}{\partial r^2} & 0 & \dfrac{\partial^2 Q}{\partial r \partial z} \\[2ex]
0 & k_\beta^2 S + \dfrac{1}{r}\dfrac{\partial Q}{\partial r} & 0 \\[2ex]
\dfrac{\partial^2 Q}{\partial r \partial z} & 0 & k_\beta^2 S + \dfrac{\partial^2 Q}{\partial z^2},
\end{bmatrix}$$

26

where:

$$P(R) = \frac{e^{-ik_pR}}{R} \qquad\qquad k_p = \frac{\omega}{v_p},$$

$$S(R) = \frac{e^{-ik_sR}}{R} \qquad\qquad k_s = \frac{\omega}{v_s},$$

$$Q(R) = S(R) - P(R) \qquad\qquad R = |\mathbf{r} - \mathbf{r}_0|.$$

For $\mathbf{r}_0 = 0$, one can observe that R as well as $P(R)$, $S(R)$ and $Q(R)$ do not depend upon the azimuthal coordinate θ.

Monopole. We consider an impulsive source, placed at the origin and acting along the z-axis. Then the cylindrical components of vector $\mathbf{a} = \hat{\mathbf{z}}$ are $[0, 0, 1]^T$. Thus the displacement can be calculated from the formula:

$$\mathbf{u}^M = \frac{\hat{F}_0}{4\pi\rho\omega^2} \begin{bmatrix} \dfrac{\partial^2 Q}{\partial r \partial z} \\[2mm] 0 \\[2mm] \dfrac{\partial^2 Q}{\partial z^2} + k_\beta^2 S \end{bmatrix} = \frac{Q}{4\pi\rho\omega^2} \begin{bmatrix} \left(\dfrac{\partial^2 Q}{\partial R^2} - \dfrac{1}{R}\dfrac{\partial Q}{\partial R}\right)\gamma_r\gamma_z \\[2mm] 0 \\[2mm] \dfrac{\partial^2 Q}{\partial R^2}\gamma_z^2 + \dfrac{1}{R}\dfrac{\partial Q}{\partial R}\gamma_r^2 + k_\beta^2 S, \end{bmatrix}$$

where $\gamma_i = \dfrac{\partial R}{\partial x_i} = \dfrac{x_i}{R}$. An important observation is that the azimuthal displacement component is equal 0, i.e. the solution is axially symmetric with respect to the z-axis. This implies, that we can model this problem using the source model of 0th order (i.e. the monopole version of the code).

Dipole. We consider an impulsive source, placed at the origin and acting along the r-axis. The cylindrical components of vector $\mathbf{a} = \hat{\mathbf{r}}$ are $[\cos\theta, -\sin\theta, 0]^T$.

Thus the displacement can be calculated from the formula:

$$
\mathbf{u}^D = \frac{\hat{F}_0}{4\pi\rho\omega^2}
\begin{bmatrix}
\left(k_\beta^2 S + \dfrac{\partial^2 Q}{\partial r^2} \right) \cos\theta \\[2ex]
-\left(k_\beta^2 S + \dfrac{1}{r}\dfrac{\partial Q}{\partial r} \right) \sin\theta \\[2ex]
\dfrac{\partial^2 Q}{\partial r \partial z} \cos\theta
\end{bmatrix}
$$

$$
= \frac{\hat{F}_0}{4\pi\rho\omega^2}
\begin{bmatrix}
\cos\theta \left(k_\beta^2 S + \dfrac{\partial^2 Q}{\partial R^2}\gamma_r^2 + \dfrac{1}{R}\dfrac{\partial Q}{\partial R}\gamma_z^2 \right) \\[2ex]
-\sin\theta \left(k_\beta^2 S + \dfrac{1}{R}\dfrac{\partial Q}{\partial R} \right) \\[2ex]
\cos\theta \left(\dfrac{\partial^2 Q}{\partial R^2} - \dfrac{1}{R}\dfrac{\partial Q}{\partial R} \right) \gamma_r \gamma_z.
\end{bmatrix}
$$

In this case, the azimuthal displacement is non-zero. The important observation here is that both u_r and u_z components of the displacement exhibit dependence of θ which is exactly given by $\cos\theta$ and the u_θ component depends upon the azimuthal coordinate through $-\sin\theta$ relationship. Comparing this with equation (14) one can see, that the pattern of the solution $\mathbf{u}^D$ corresponds to the solution $\hat{\mathbf{u}}_n$ up to the multiplication of the second component of $\mathbf{u}^D$ by factor $-i$.

This means that one can use a dipole version of the code (with $n = 1$) for the solution of elastic wave propagation problem with the exact solution given in trace domain (i.e. (r, z)-plane) by:

$$
\mathbf{u}^D(r, z) = \frac{\hat{F}_0}{4\pi\rho\omega^2}
\begin{bmatrix}
\left(k_\beta^2 S + \dfrac{\partial^2 Q}{\partial R^2}\gamma_r^2 + \dfrac{1}{R}\dfrac{\partial Q}{\partial R}\gamma_z^2 \right) \\[2ex]
i\left(k_\beta^2 S + \dfrac{1}{R}\dfrac{\partial Q}{\partial R} \right) \\[2ex]
\left(\dfrac{\partial^2 Q}{\partial R^2} - \dfrac{1}{R}\dfrac{\partial Q}{\partial R} \right) \gamma_r \gamma_z.
\end{bmatrix}
$$

For both monopole and dipole cases, the problem is solved with Neumann boundary conditions prescribed at the edge of a circular hole surrounding the

source, where the corresponding tractions are computed using the analytical solution. We used the same geometry settings as for the acoustic case.

Sample results of simulations for the acoustic dipole at frequency 25 kHz, are shown in Figures 10 and 9. The final optimal fine hp mesh is presented in Figure 9a. Figure 9 displays the real part of displacement components: u_r (subfigure (a)), u_z (subfigure (b)), and u_θ (subfigure c), along with corresponding (logarithms of modules of) differences between calculated and analytical solutions. In addition, we show the behavior of the solution in the PML layer along profile Q defined in Figure 3.

Similarly to the acoustic case, we observe finer meshes in the PML region. The difference between calculated and analytical solution is of order 10^{-7} or less where the solution magnitude of order 10^{-2}. Higher discrepancies are observed within the PML layer. All three components of the displacement are efficiently damped by the PML and attain machine zero at two thirds of the PML depth.

The remaining examples are presented in Appendix Appendix B: with the monopole point source at frequency 50 Hz for both formulations (Figures B.37, B.38, B.40 and B.39). and 25 kHz for both formulations (Figures B.41, B.42, B.44 and B.43), with the dipole source at frequency 50 Hz for formulation B (B.45, B.46, B.48 and B.47) and 10 kHz (Figures B.50 and B.49).

Similar observations to those for pure acoustic problem can be made: the hp algorithm produces different meshes for low and high frequencies. The convergence rate is at least algebraic (Figures 11, 12, 13, 14). For all tested cases the PML efficiently damps the solution to the machine zero value and thus enables to accurately solve the elastic wave propagation problem for the homogenous elastic material for the range of frequencies from 50 Hz to 25 kHz.

(a) Fine mesh

(b) $\mathrm{Re}(u_r)$, $\mathrm{Re}(u_z)$ and $\mathrm{Re}(u_t heta)$ along the profile (zoomed in PML zone, PML marked in blue)
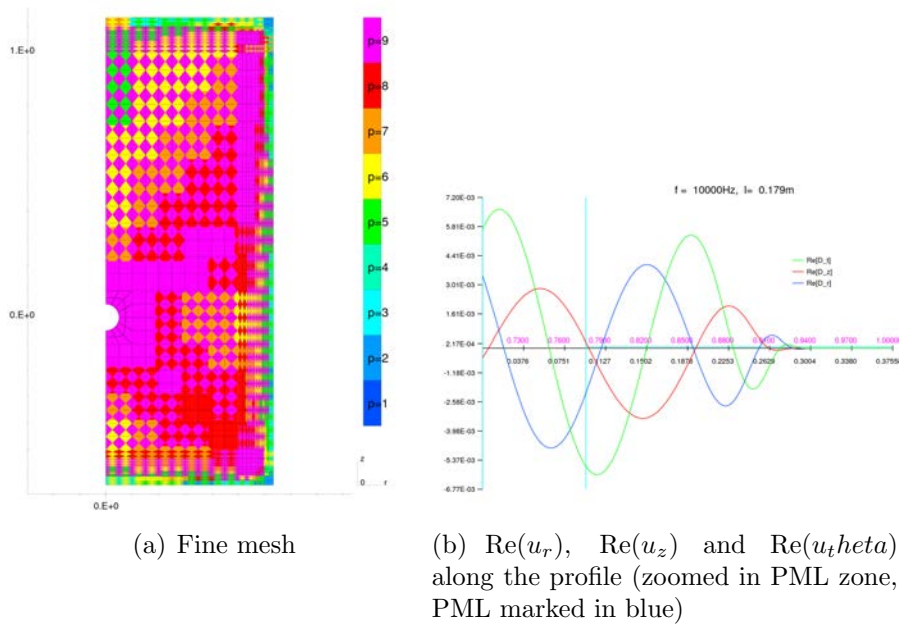
Figure 9: Elasticity. Dipole point source. Formulation A. $f = 10$ kHz

(a) $\mathrm{Re}(u_r)$

(b) $\mathrm{Re}(u_z)$

(c) $\mathrm{Re}(u_\theta)$

(d) $\log \left| u_r^f - u_r^{ex} \right|$

(e) $\log \left| u_z^f - u_z^{ex} \right|$

(f) $\log \left| u_{\theta^f} - u_{\theta^{ex}} \right|$
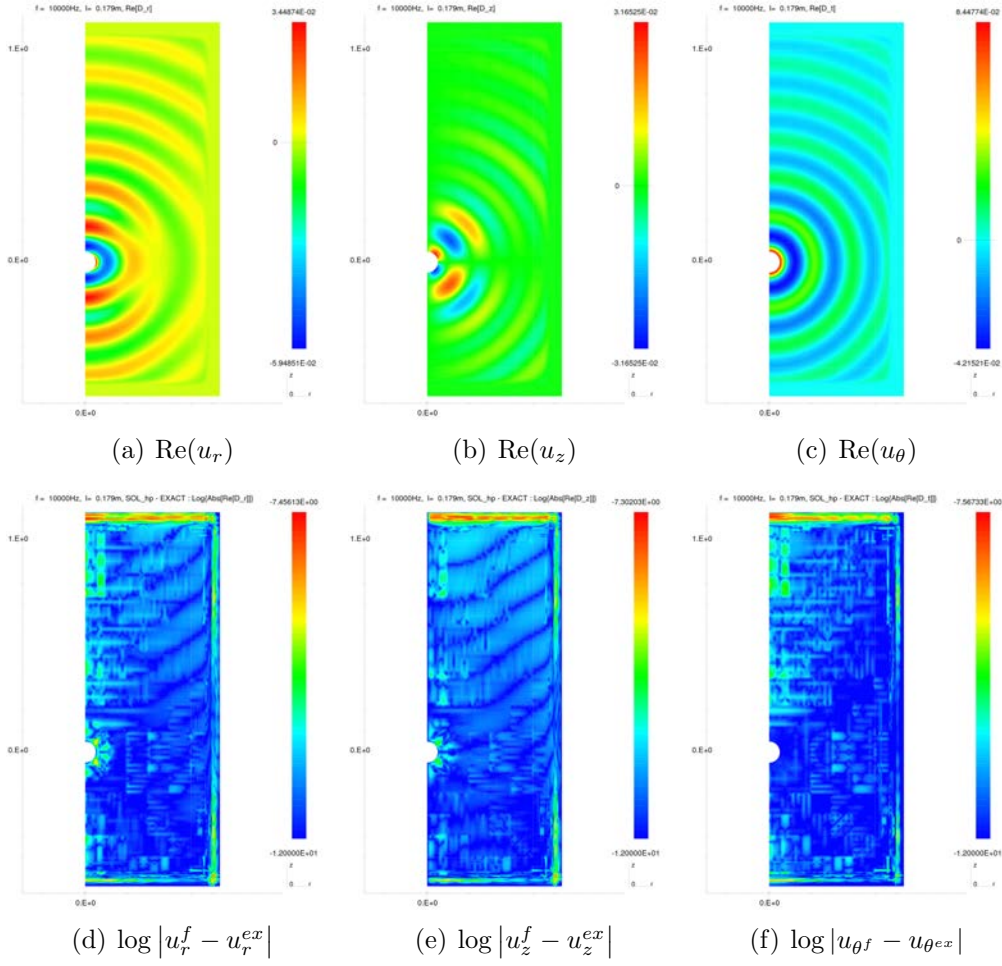
Figure 10: Elasticity. Dipole point source. Formulation A. $f = 10$ kHz
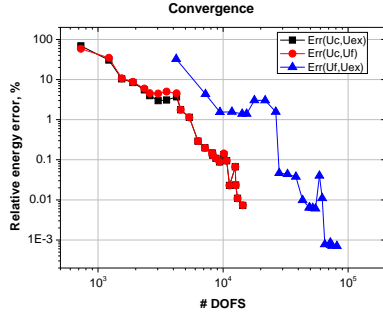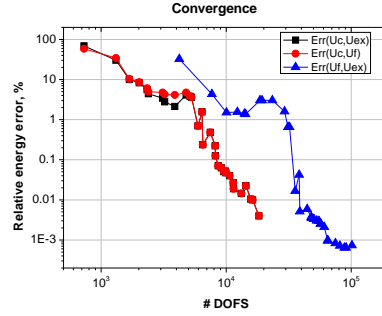
(a) Formulation A (b) Formulation B

Figure 11: Convergence for elasticity. Monopole point source. $f = 50$ Hz
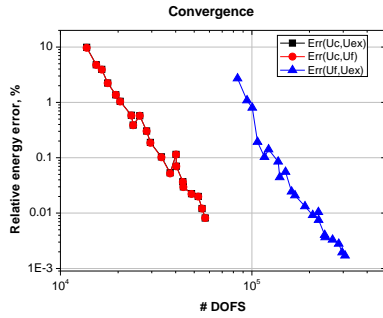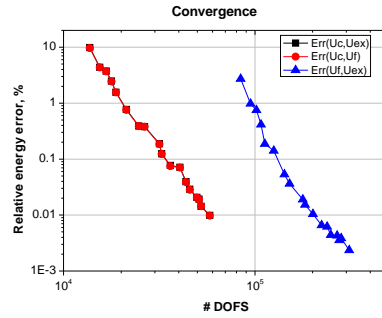
(a) Formulation A (b) Formulation B

Figure 12: Convergence for elasticity. Monopole point source. $f = 25$ kHz

4.4. Coupled case

Verification of the code for the coupled case was performed using another approach. For the purpose of comparison, instead of using an analytical solution, we used another 1D semi-analytical code [29] which calculates solutions for simple geometries according to the mathematical procedure described in [11, 12]. As an alternate to the comparison of pressure and displacement within the computational domain, we chose to compare the waveforms and dispersion curves obtained by postprocessing the direct results of the simulations for the whole range of frequencies. The approach enables to verify the complete method (i.e. simulation of the problem for the whole range of frequencies and the transformation of the solution into the time domain using

32

(a) Formulation A (b) Formulation B
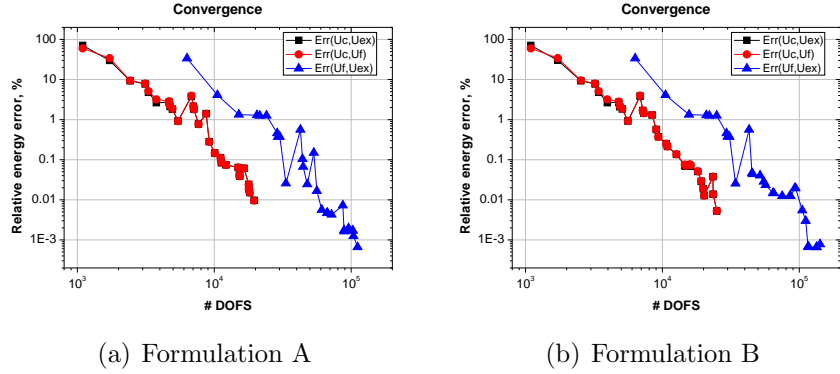
Figure 13: Convergence for elasticity. Dipole point source. $f = 50$ Hz

(a) Formulation A (b) Formulation B
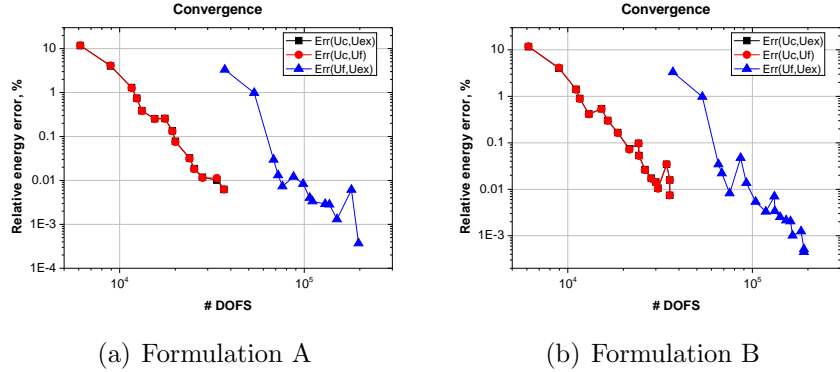
Figure 14: Convergence for elasticity. Dipole point source. $f = 10$ kHz

fast inverse Fourier transform) and, additionally, gives a physical verification of the method by clear exposition of the different kinds of waves that are generated in the formation and the borehole.

We considered two geometrical cases: with open borehole (Figure 15(a)), and the presence of the solid elastic wireline tool, centered in the borehole (Figure 15(b)). Inside the borehole we put the acoustic source and the array of 8 equally spaced receivers (spacing equal 0.15 m). The simulations were performed for fast and slow homogeneous formations. Physical parameters for the materials used in the calculations are summarized in Table 2. In all cases we set quality factors to ∞, i.e. we assume no attenuation in the materials. We considered two kinds of acoustic sources: monopole and dipole source, both being Ricker wavelets with a central frequency of 8603 Hz.

(a) Open borehole   (b) With the solid wireline tool
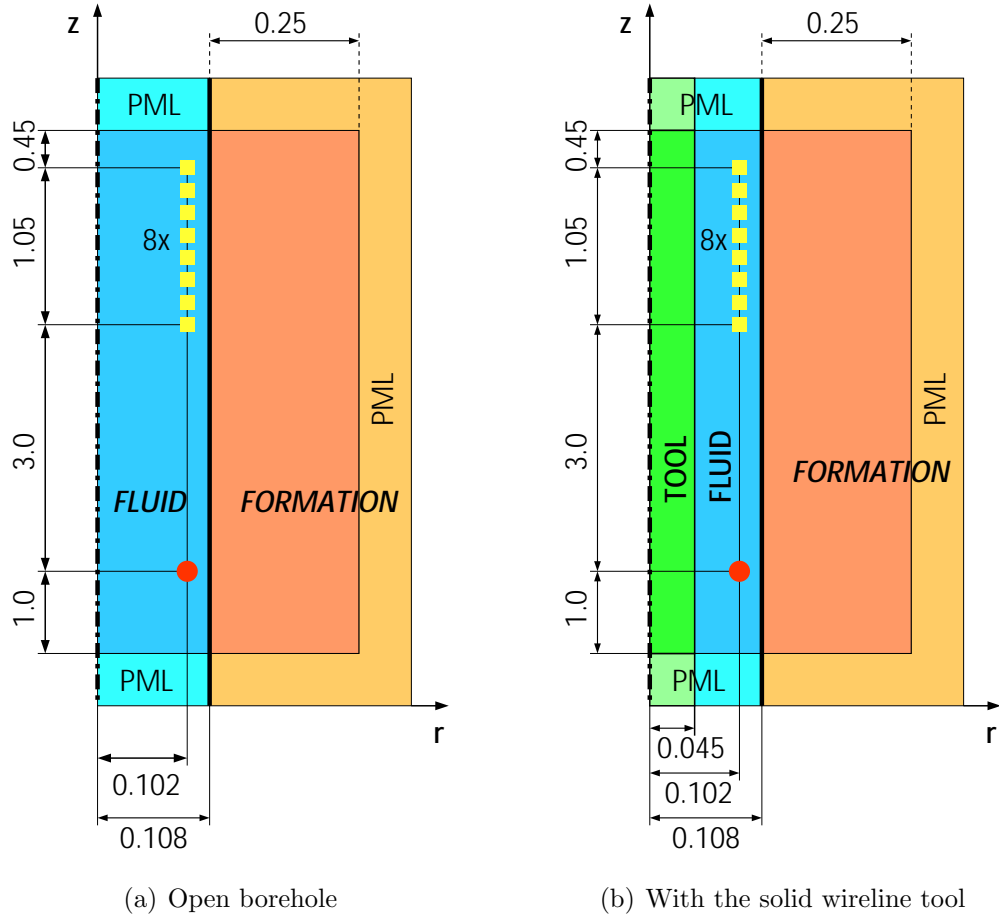
Figure 15: Geometries for the coupled problems. All the dimensions in meters.

The first example deals with the modeling of a homogeneous fast formation for a monopole source at central frequency 8603 Hz. The obtained waveforms are presented in Figure 16. The thick curves are obtained from 1D semianalytical code, whilst the thin ones are coming from the hp-adaptive FEM calculations. In both cases: without a tool (subfigure (a)) and in presence of the tool (subfigure (b)), we can easily identify S-wave (indicated by S) and Stoneley wave package (indicated by St) arrivals, respectively. The P-wave mode, although present (see the dispersion curves in Figure 17a), is not clearly visible because its amplitude is very small in comparison to the Stoneley mode. Due to the amplitude comparison, most of the wave energy

	P-wave		S-wave		Density
	$V_p\ [m/s]$	$1/V_p\ [\mu s/ft]$	$V_s\ [m/s]$	$1/V_s\ [\mu s/ft]$	$\rho\ [kg/m^3]$
fluid	1524	200.0	–	–	1100
fast form.	3048	100.0	1793	170.0	2200
slow form.	2300	132.5	1000	304.8	2000
tool	5860	52.0	3130	97.4	7800

Table 2: Material parameters used in verification of the code for coupled problems.

is carried by the dominant Stoneley mode. In the presence of the tool however, we are also able to identify a very weak mode which is a superposition of the tool S-wave (indicated by *TS*) and the formation P-wave. Another noticeable change between these two cases is the variation in a shape of the Stoneley mode, but not in the time arrival of this mode.

Comparison of the dispersion curves obtained for both cases (Figure 17) also confirms existence of the mentioned modes. This kind of presentation of the existing modes gives a direct insight into the nature of the modes and makes possible to instantly estimate the slowness and character of the modes, which is of a primary importance for recovering information about elastic parameters of the formation. Thus we see, for the whole range of frequencies, the slowest, weakly dispersive Stoneley mode which additionally exhibits anomalous dispersivity (dispersion curve has negative slope). The mode is characteristic for the fast formation.

The following (pink) dispersive mode is the pseudo-Rayleigh mode. It begins at the cutoff frequency and drops from formation S-wave velocity to approach the fluid wave speed at high frequencies. Very weak formation P-wave mode is seen for the case without the tool (subfigure (a)). In the presence of the tool, a corresponding tool mode (orange-pink) appears in subfigure (b).

The second example deals with the modeling of a homogeneous slow formation for a monopole source at central frequency 8603 Hz. The waveforms are presented in Figure 18. In both cases (without a tool — subfigure (a), and with the tool — subfigure (b)), we can easily identify P-wave (indicated by *P*) and Stoneley wave packages (indicated by *St*) arrivals, respectively. Obviously, the time arrivals of the wave packages are delayed in comparison to the fast formation. Lack of the S-wave agrees with the theory: in the slow formation, S-wave velocity falls below the speed of sound in the borehole fluid, and thus refraction of the shear head wave is impossible. In the

presence of the tool however, an additional tool mode (indicated by *TP*) introduces some disturbance into the formation P-wave arrival.

The corresponding dispersion plots (Figure 19)) clearly identify the actual modes. As for the fast formation, the Stoneley mode is dominant. The mode is weakly dispersive at higher frequencies and it exhibits a larger dispersivity at the low frequency limit. The P-wave mode is clearly visible in both cases, and so is the tool mode in the case with the tool present.

The next example deals with the modeling of a homogeneous fast formation for a dipole source at central frequency 8603 Hz. The waveforms are presented in Figure 20. For both cases, one can identify arrivals of the S-wave and highly dispersive flexural wave packages (indicated by *F*). In the presence of the tool (subfigure (b)), an additional, perturbed by the tool, formation P-wave arrival can be observed. The dispersion plot (Figure 21a) for the open borehole indicates existence of the first two flexural modes (the 1st in yellow, and the 2nd in blue/red). The important feature of the flexural modes is that its phase velocity drops from the formation S-wave velocity at the cutoff frequency, which makes this type of sonic measurement a useful tool in estimating elastic parameters of the formation. In the presence of the tool, an additional tool mode is present (Figure 21b).

The last example focuses on the modeling of a homogeneous slow formation for a dipole source at central frequency 8603 Hz. The waveforms are presented in Figure 22. For both cases one can identify arrivals of the P-wave and flexural wave packages. In the presence of the tool (subfigure (b)), the P-wave package is perturbed by the tool modes. The dispersion plot (Figure 23a) for the open borehole indicates existence of the first flexural modes (yellow) and the P-wave mode (red). The flexural mode begins at S-wave speed at low frequencies which makes possible to pick up the formation S-wave slowness despite the fact that the formation S-wave is not observed in waveforms. In the presence of the tool, an additional tool mode is observed (Figure 23b).

In all the presented cases, the dispersion curves and waveforms, calculated via postprocessing solutions from the *hp* simulations, perfectly match the results obtained with the 1D semi-analytical method. This confirms the high accuracy of the *hp* elements and builds up the confidence in the method.
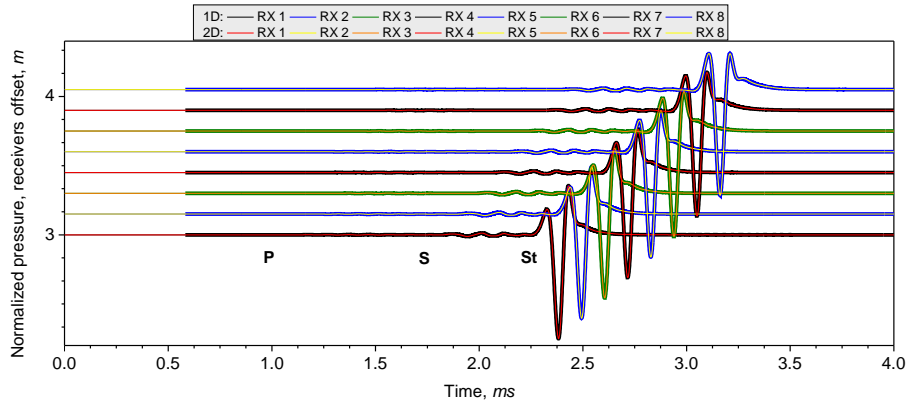
(a) Open borehole
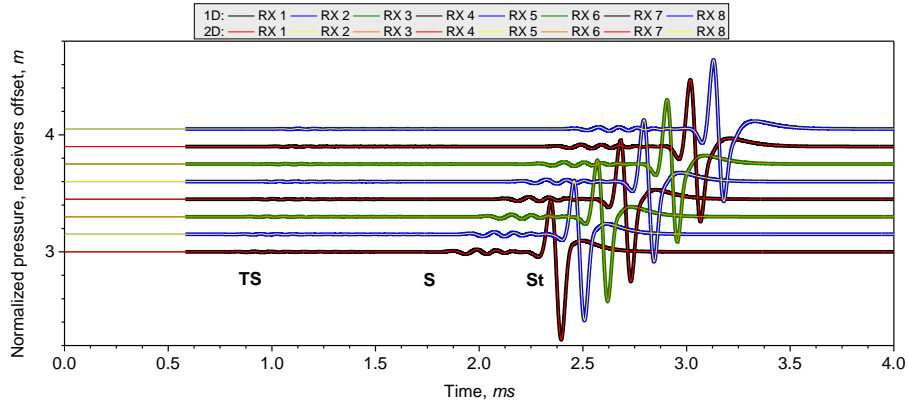
(b) With wireline tool

Figure 16: Waveforms for monopole source and fast formation.

5. Representative examples

5.1. Fast formation with a soft layer

The geometry of the first nontrivial example is shown in Figure 24. Outside of the open borehole, and within the the fast formation, there is a soft layer of thickness 0.5 m. The radial thickness of the formation, excluding the PML layer, is equal 25 cm.

We consider two positions of the array of 13 receivers: the first (left subfigure), where the array is facing the soft layer and the second (right subfigure), where the array of receivers is placed in between the acoustic

(a) Open borehole   (b) With wireline tool
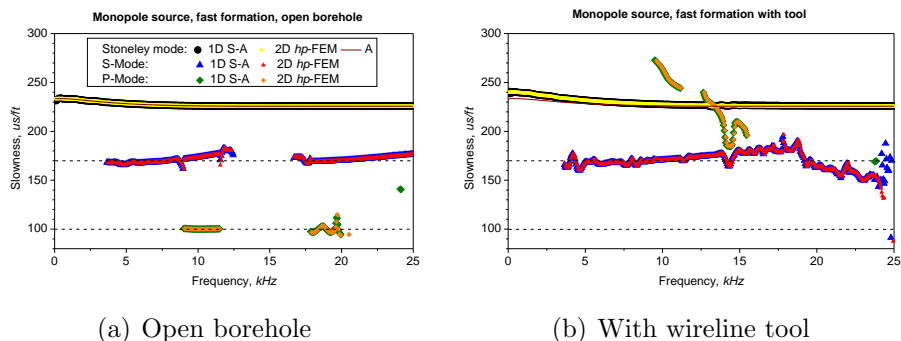
Figure 17: Dispersion curves for monopole source and fast formation.

	P-wave		S-wave		Density
	V_p $[m/s]$	S_p $[\mu s/ft]$	V_s $[m/s]$	S_s $[\mu s/ft]$	ρ $[kg/m^3]$
fluid	1524	200.0	−	−	1100
slow form.	2300	132.5	1000	304.8	2000
fast form.	3048	100.0	1793	170.0	2200

Table 3: Material parameters describing the problem with layers: density ρ, speeds of waves V and corresponding slownesses S.

source and the soft layer. Material parameters describing formation and fluid are given in Table 3.

The simulation was performed for monopole and dipole acoustic sources at central frequency 8603 Hz.

Figure 25 shows the waveforms obtained for the monopole and dipole source, respectively. The waveforms obtained for the first position (in the subfigures on the left) can be divided into three groups.

The first group, corresponding to the first 6 receivers, exhibits the most complicated behavior. The first wave package consists of P-wave, S-wave and Stoneley (for monopole) or flexural (for dipole) modes. After this package, one can observe two similar, weaker and recorded in reverse order wave packages. These correspond to the reflected P- and S-waves from the two horizontal interfaces bounding the soft layer.

The second group, corresponding to the last 5 receivers, exhibit typical behavior for the fast formation: one can observe arrivals of the P-, S- and Stoneley/flexural modes. However, in comparison to the arrivals observed in the first waveform group, the arrivals for the last receivers are slightly
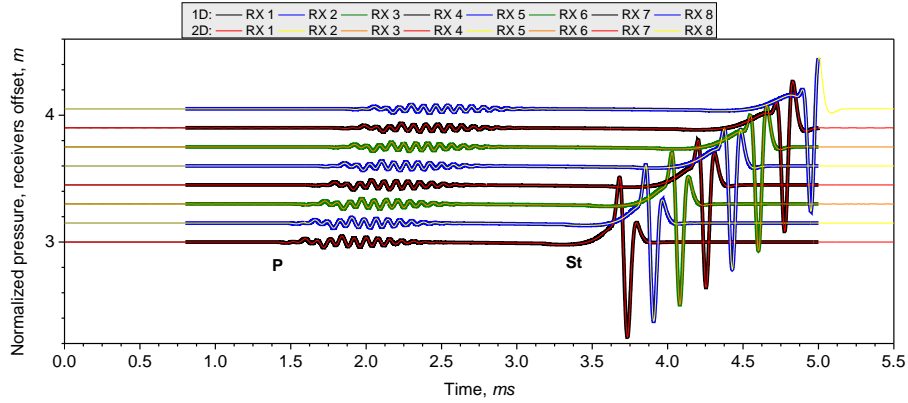
(a) Open borehole
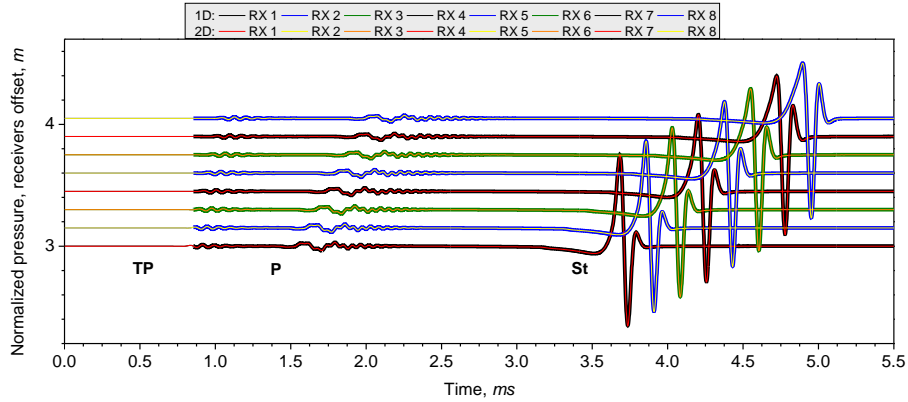
(b) With wireline tool

Figure 18: Waveforms for monopole source and slow formation.

delayed due to the presence of the slow formation layer. After the main wave package, one can observe very weak, additional waves. These are multiply reflected (trapped in the soft layer) waves.

The third group of waveforms, corresponds to the central receivers, facing directly the soft layer. In here one can clearly discriminate only fast formation P-wave arrivals.

The waveforms obtained for the second position (subfigures on the right) exhibits a similar behavior. Analogously to the first group of waveforms for the position 1, we one can observe arrivals of the direct P-, S- and Stoneley/flexural modes, followed by two packages of the reflected waves.

(a) Open borehole   (b) With wireline tool
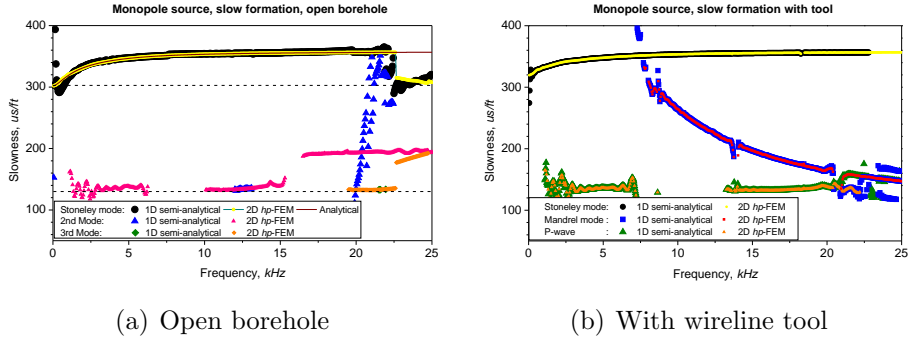
Figure 19: Dispersion curves for monopole source and slow formation.

Figure 26 shows the results of the dispersion processing, obtained for the monopole and dipole source, respectively. Left subfigures displays curves calculated for the position 1. In that case, it is nearly impossible to recover any meaningful information about the physical parameters of the formation due to the superposition of the direct and multiply reflected waves. The extended Prony method, used for dispersion processing, is unable to detect the existing modes, when different subsets of receivers collect data containing different acoustic modes.

On the other hand, the dispersion processing is successful in the second case where all the receivers obtain a similar information.

In the case of the monopole acoustic source, one can identify the slowest Stoneley mode (with characteristic for the fast formation anomalous dispersivity) and the pseudo-Rayleigh mode (beginning slightly above the S-wave slowness S_3 of the fast formation). One can also observe highly dispersive modes (vertical lines) which corresponds to the reflected waves.

Similarly, for the dipole case, one can also identify the first and the second flexural modes, both of them beginning slightly above the S-wave slowness S_3 of the fast formation. The curves corresponding to the reflected waves are present in this case as well.

5.2. Logging while drilling

The next example deals with the simulation of the sonic logging-while-drilling (LWD) scenarios for the homogeneous fast and slow formations. In comparison to the wireline tool, which is modeled as a solid cylinder occupying a part of the borehole, the LWD tool possesses an internal fluid filled
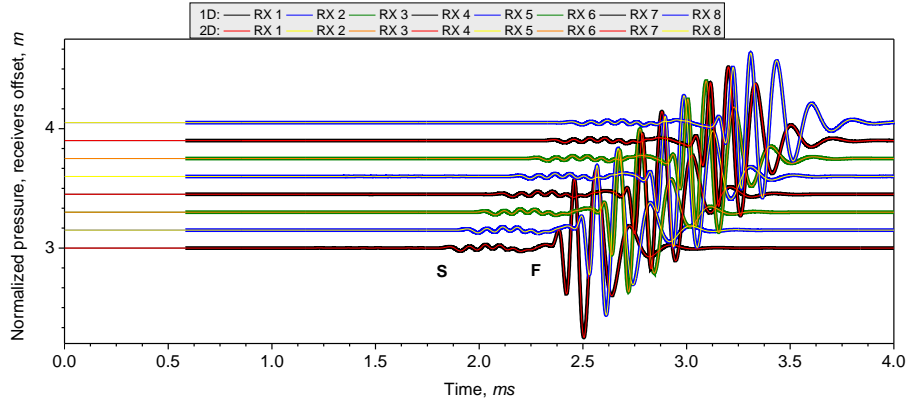
(a) Open borehole
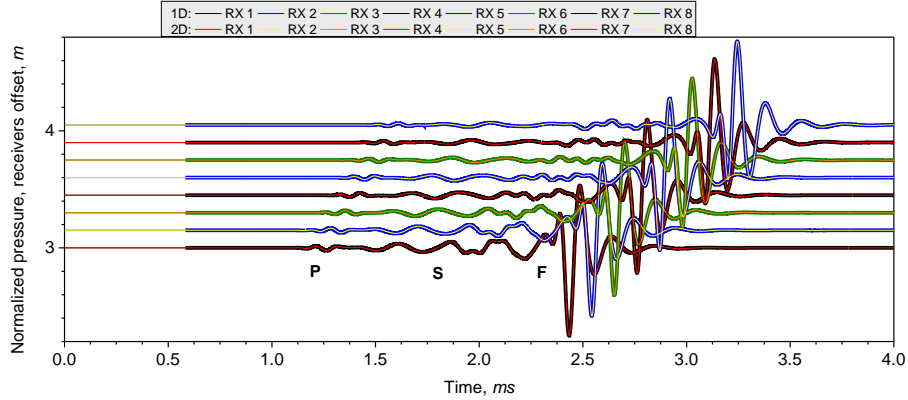
(b) With wireline tool

Figure 20: Waveforms for dipole source and fast formation.

channel and occupies a much larger portion of the borehole. The smaller annulus filled with the fluid, as well as the additional vertical fluid filled channel changes significantly the wave propagation environment.

The geometry for the problem is shown in Figure 27. Material parameters describing two kinds of formations and fluids are given in Table 4. In the case of the monopole source, we used excitation at central frequency equal 8000 kHz. For the dipole and quadrupole acoustic source, we used excitation at central frequency equal 3500 kHz.

Figure 28 shows the waveforms obtained for the fast and slow formation, respectively. In each case, we present the results obtained for a monopole,

	Dipole source, fast formation, no tool	Dipole source, fast formation with tool
(a) Open borehole		(b) With wireline tool
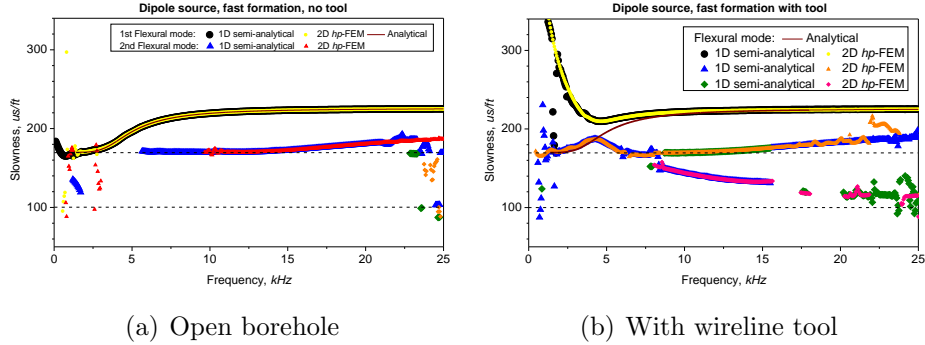
Figure 21: Dispersion curves for dipole source and fast formation.

	Id	P-wave		S-wave		Density
		V_p $[m/s]$	S_p $[\mu s/ft]$	V_s $[m/s]$	S_s $[\mu s/ft]$	ρ $[kg/m^3]$
tool	1	5862	52.0	2519	121.0	7800
slow form.	2	2300	132.5	1000	304.8	2000
fast form.	2	3048	100.0	1793	170.0	2200
fluid	3	1500	203.2	−	−	1100

Table 4: Material parameters describing the LWD problems: density ρ, speeds of waves V and corresponding slowness S.

dipole and quadrupole acoustic sources.

For the monopole source, the first wave to arrive is a collar wave. For the fast formation, it is weaker and simpler in shape. For the soft formation, the wave is more prominent and more complicated in shape due to the superposition of stronger formation P-wave waveforms. In the fast formation, one can further observe a weak, but distinguishable, arrival of formation S-wave package, followed by the strongest Stoneley mode. In the slow formation, the Stoneley mode can be observed as the last and the strongest waveform component. It is also delayed, when compared with the fast formation.

For the dipole source and the fast formation, one can see only the arrival of the dispersive formation flexural mode. The waveforms obtained for the slow formation are clearly separated into two groups: a highly dispersive collar mode, followed by the formation flexural mode.

In the case of a quadrupole acoustic source, for both fast and slow formations, one can observe only one wave package which corresponds to the formation quadrupole (screw) mode. The arrival time of this mode corre-
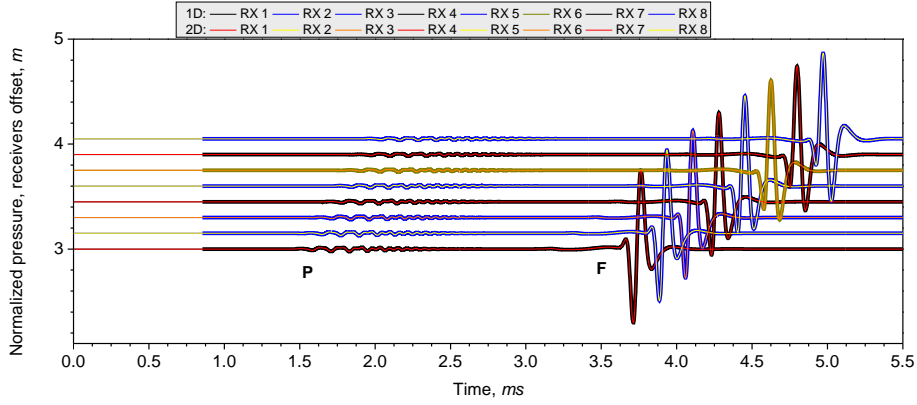
(a) Open borehole
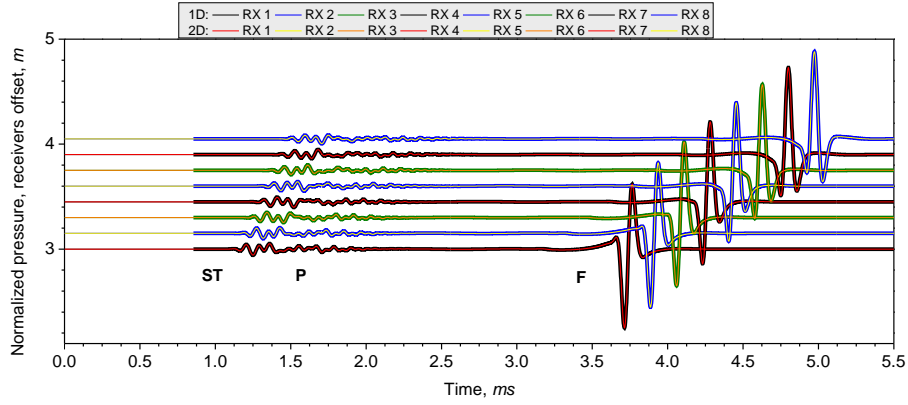
(b) With wireline tool

Figure 22: Waveforms for dipole source and slow formation.

sponds to the anticipated formation S-wave arrival.

Figure 29 show the results of the dispersion processing, obtained for the fast and the slow formations, respectively. In each case, we present the results obtained for a monopole, dipole and quadrupole acoustic source.

Comparing dispersion curves obtained for a monopole acoustic source, one can see a similar character of some curves. The topmost, slightly dropping curves, existing for all the frequencies, correspond to the formation Stoneley mode. The Stoneley mode in the slow formation propagates with a lower velocity. The second, deflecting curve, which exhibit exactly the same character for both formations, corresponds to the collar monopole mode. In

(a) Open borehole (b) With wireline tool
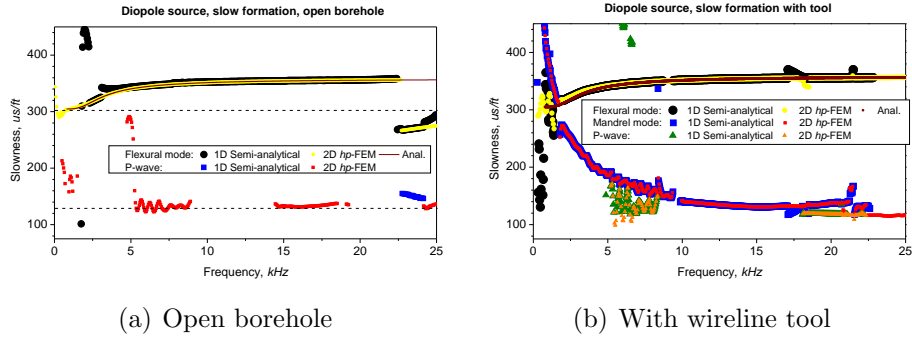
Figure 23: Dispersion curves for dipole source and slow formation.

addition, for the fast formation, one can clearly identify the nondispersive S-wave curve.

In the case of the dipole acoustic source, the situation is more complicated. The reason for it is that the curve corresponding to the first flexural mode crosses with highly dispersive collar mode at a low frequency (c.a. 1 kHz) and thus produces a complex wave behavior in low frequencies. Here, the dispersion processing software was not able to discriminate these two curves: instead having two crossing curves, one ended up with two separate curves with some lag between them. Each of the curves is composed of fragments of flexural and collar curves. For the case of the fast formation, a separate curve corresponding to the formation S-wave mode is present. In the case of the slow formation, picking up the formation S-wave slowness is impossible, due to the lack of the low frequency part of the 1st flexural mode.

Such a problem does not occur for the quadrupole acoustic source. The quadrupole collar mode is well separated from the formation screw mode, because the collar mode begins at some cut-off frequency, which is beyond the excitation frequency range of the source. Thus, one can clearly identify the dispersive formation quadrupole mode, which begins at formation S-wave slowness at low frequency. For the fast formation, the independent S-wave mode exists, manifesting itself in an additional dispersion curve.

6. Conclusions

A summary. The paper is a continuation of [1] and focuses on extending the fully automatic *hp* FE methods to coupled acoustic/anelasticity problems. The methodology is applied to a challenging problem of modeling sonic tools
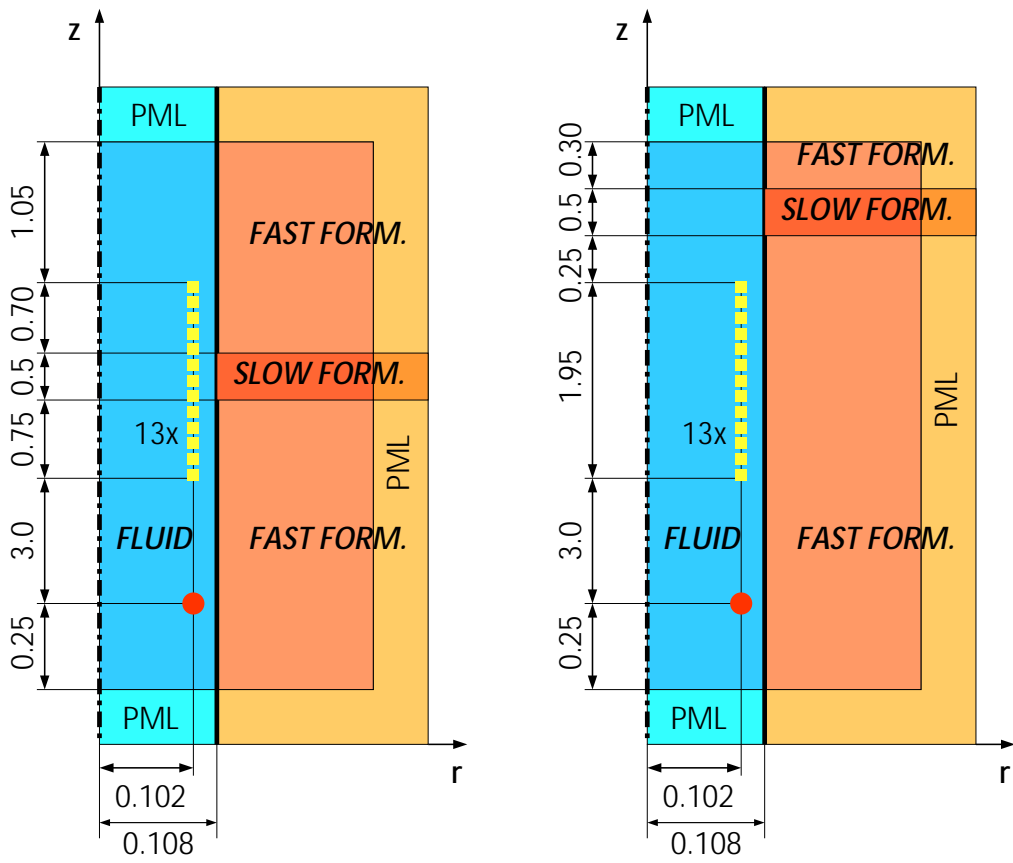
Figure 24: Geometry of the problem with soft layer. Two positions of the array of receivers.

(a) Monopole, position 1

(b) Dipole, position 1

(c) Monopole, position 2

(d) Dipole, position 2
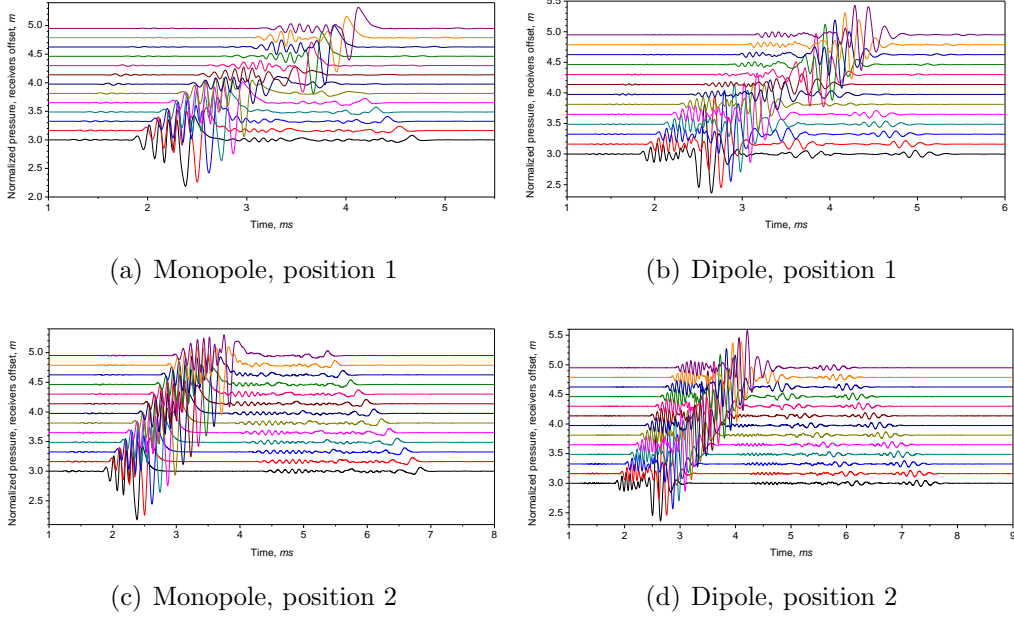
Figure 25: Problem with layers: waveforms for the monopole and dipole source.

in the borehole environment. The extension of adaptive hp-algorithm to coupled problems required an automatic energy rescaling procedure. The method delivers a superior accuracy compared with non-adaptive discretization schemes (including Finite Differences) and we have documented the claim with a careful verification of the methodology and the code. Finally, we have presented a number of non-trivial examples illustrating the potential of the hp-technology.

Challenges and future work. It would be a lie to claim that we have not encountered any problems. The main challenge comes from the construction of Perfectly Matched Layer and its mathematical understanding. The PML method is practically the only technique that we can think of in the case of geometries involving multiple layers and the borehole. The construction of the implemented PML extrapolates heavily from a simple 1D case and seems to be insufficient in the case of waveguide geometries, especially in context of coupled problems and anisotropies [30]. We have not experienced these problems in the examples presented in this paper.

Our current work is marching in two directions. Non-axisymmetric ge-

(a) Monopole, position 1

(b) Dipole, position 1

(c) Monopole, position 2

(d) Dipole, position 2
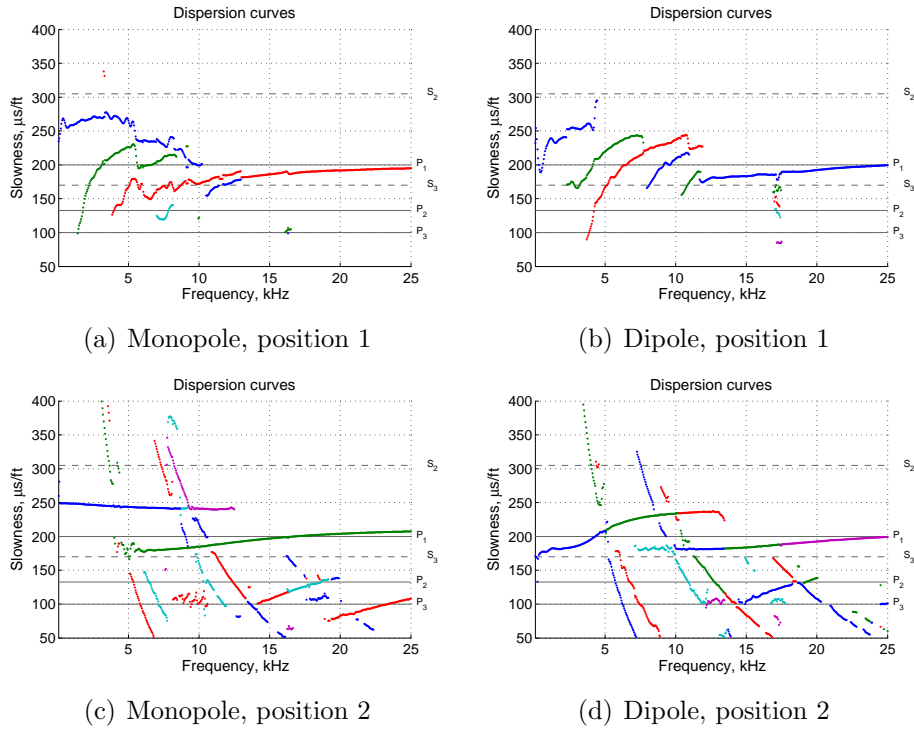
Figure 26: Problem with layers: dispersion curves for the monopole source.

ometries call for the use of 3D elements and the 3D implementation is indeed underway. On the modeling side, we focus on more sophisticated models for the formation including various poroelasticity theories. We hope to report new results soon in a forthcoming paper.

Appendix A. Verification of the acoustic part of the code
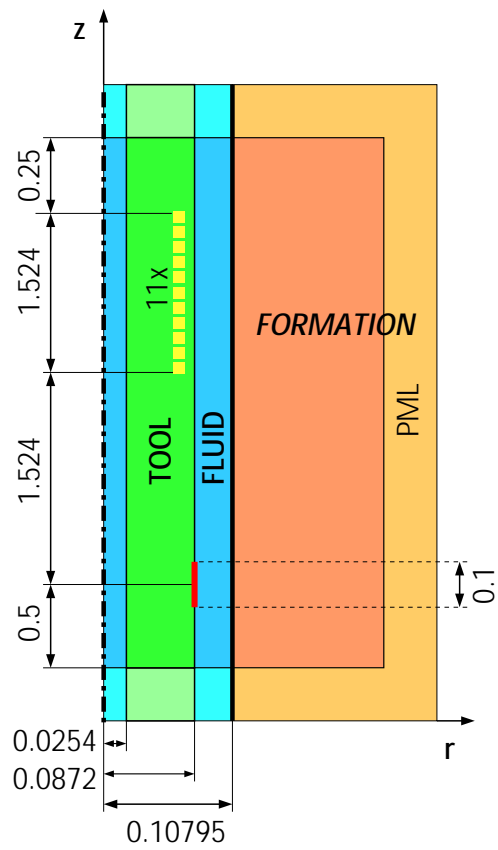
Figure 27: Geometry of the LWD problem.
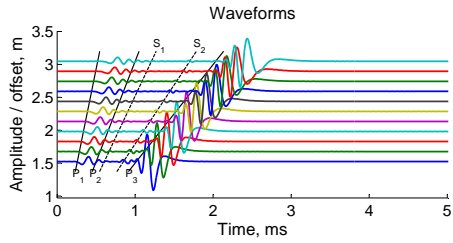
(a) Fast formation, monopole
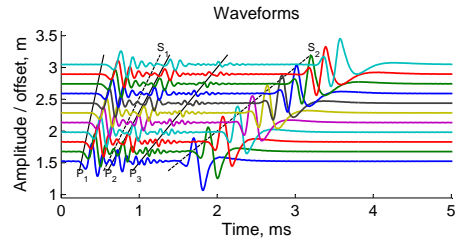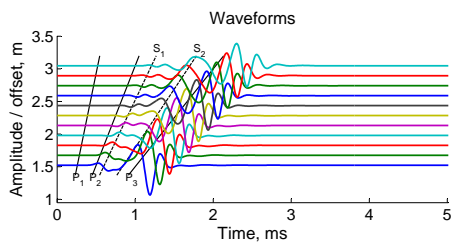
(b) Slow formation, monopole

(c) Fast formation, dipole
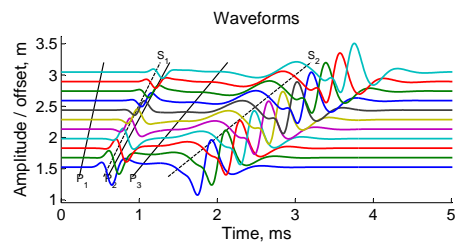
(d) Slow formation, dipole
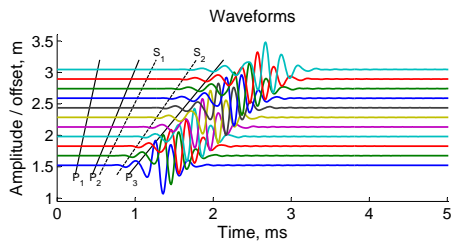
(e) Fast formation, quadrupole
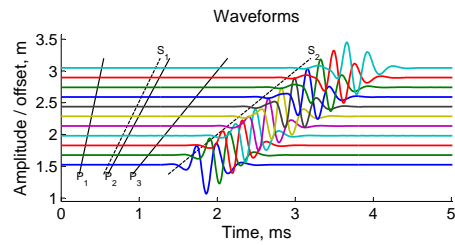
(f) Slow formation, quadrupole

Figure 28: Waveforms obtained for LWD problem with homogeneous fast formation and different acoustic sources. P and S with indices (see Table 4) indicate appropriate arrivals of P- and S-waves.

49
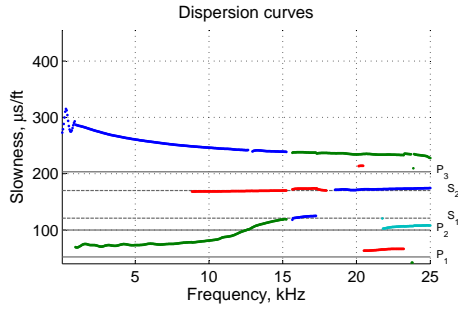
(a) Fast formation, monopole
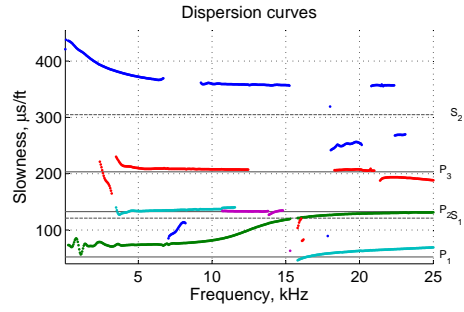
(b) Slow formation, monopole
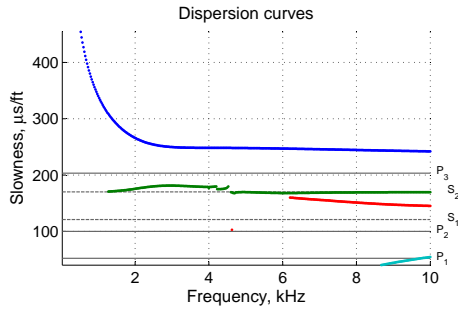
(c) Fast formation, dipole
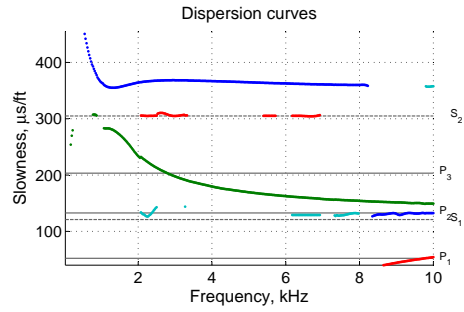
(d) Slow formation, dipole
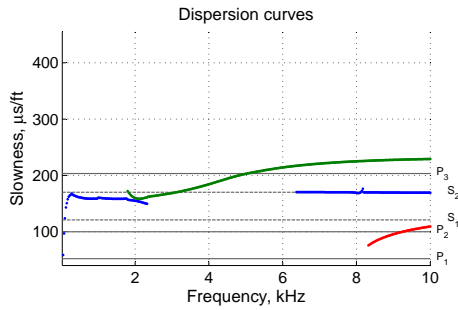
(e) Fast formation, quadrupole
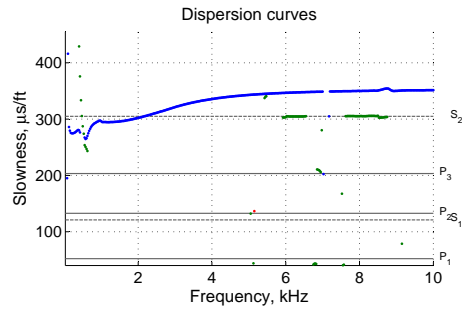
(f) Slow formation, quadrupole

Figure 29: Dispersion curves obtained for LWD problem with homogeneous fast formation and different acoustic sources. P and S with indices (see Table 4) indicate appropriate arrivals of P- and S-waves.

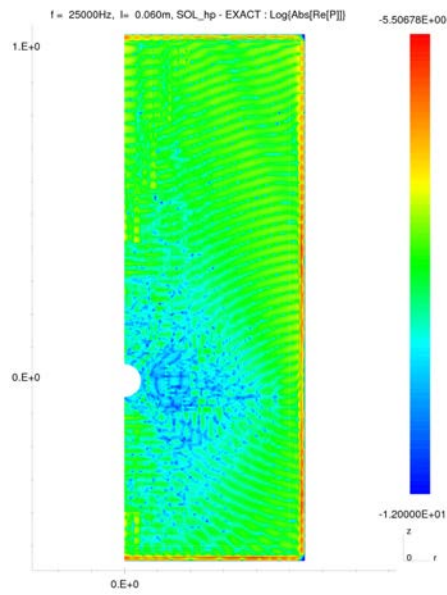50
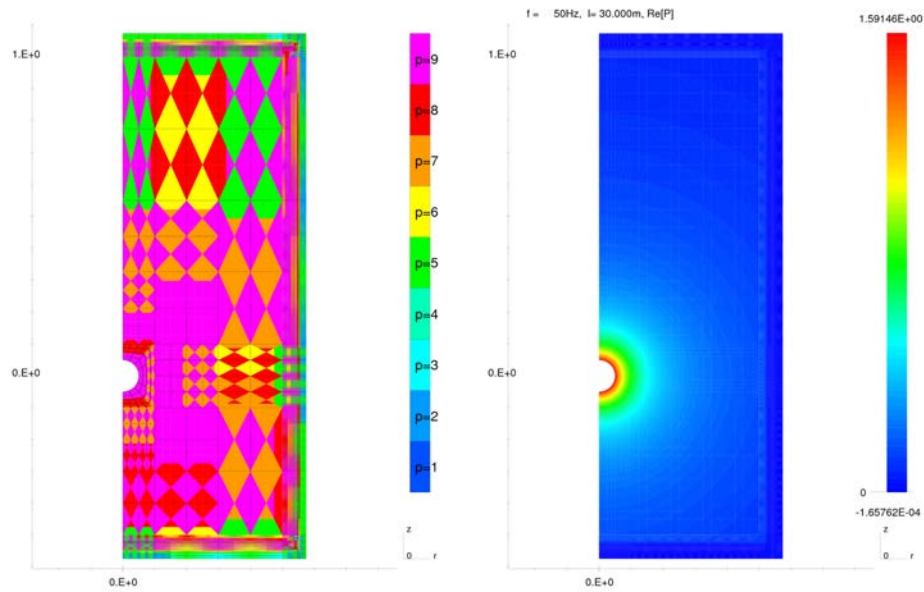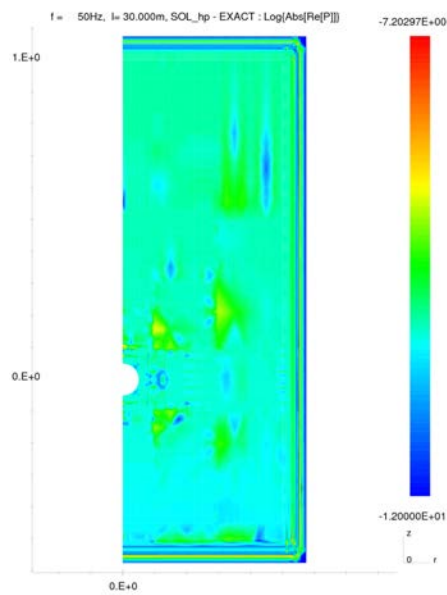
(a) Fine mesh
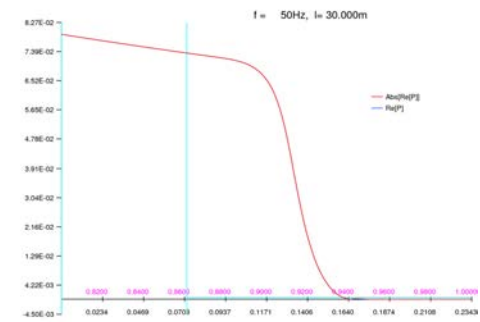
(b) Re(p)

(c) $\log |p_f - p_{ex}|$

(d) Re(p) (red) and $|p|$ (blue) along the profile (zoomed in PML zone, PML marked in blue)

Figure A.30: Acoustics. Monopole point source. Formulation A. $f = 50$ Hz
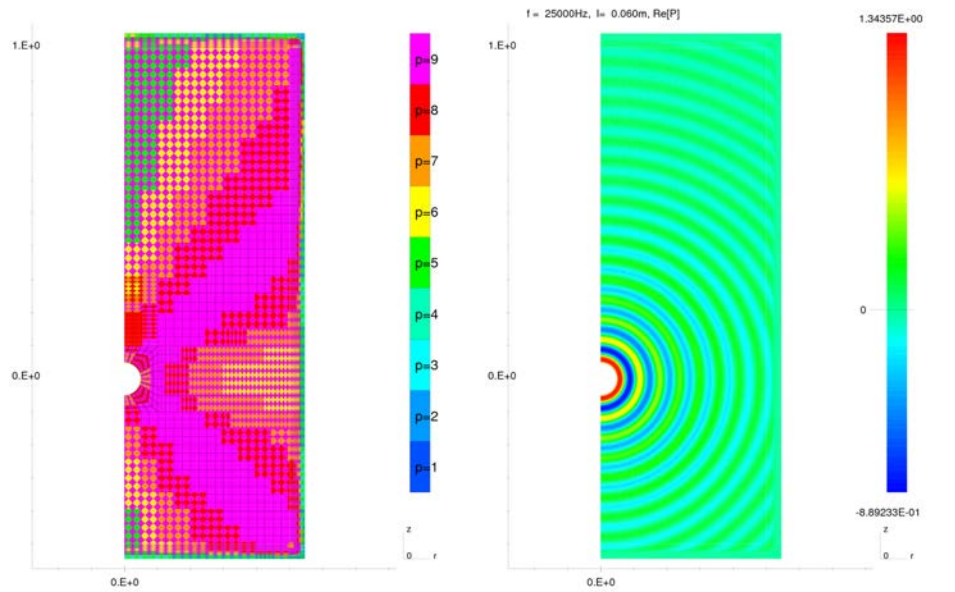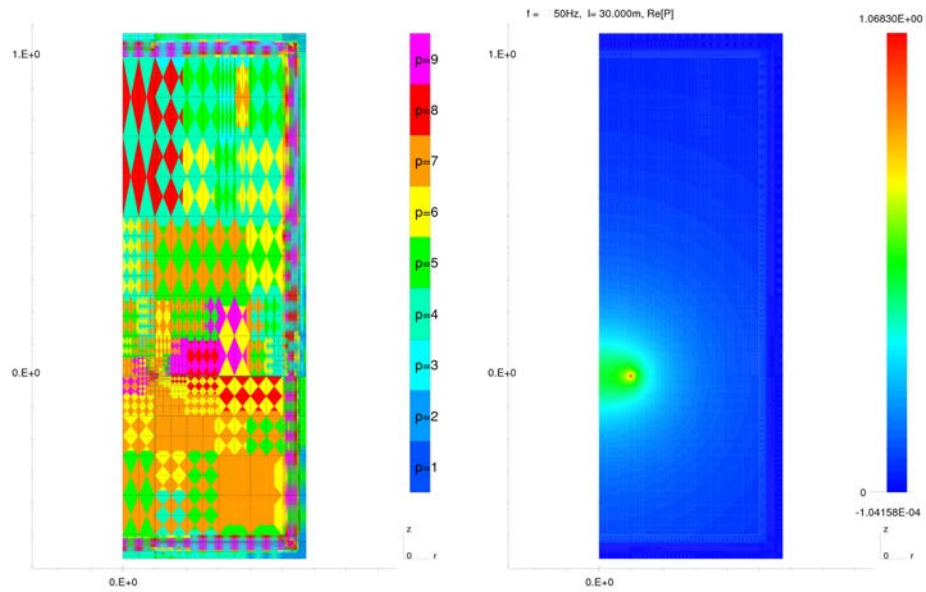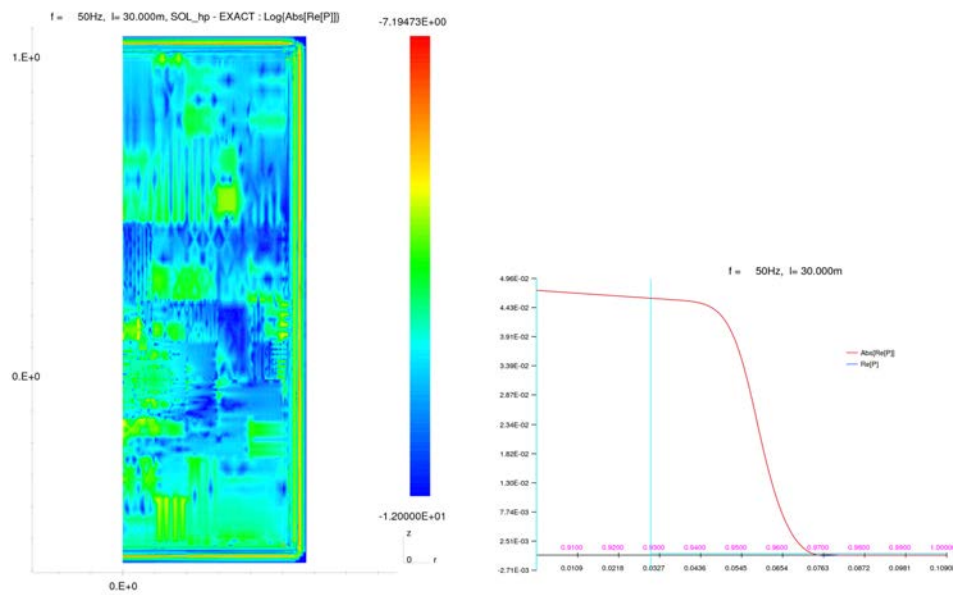
51

(a) Fine mesh

(b) Re(p)

(c) $\log |p_f - p_{ex}|$

(d) Re(p) (red) and $|p|$ (blue) along the profile (zoomed in PML zone, PML marked in blue)

Figure A.31: Acoustics. Monopole point source. Formulation A. $f = 25$ kHz

(a) Fine mesh

(b) Re(p)

(c) $\log |p_f - p_{ex}|$

(d) Re(p) (red) and $|p|$ (blue) along the profile (zoomed in PML zone, PML marked in blue)

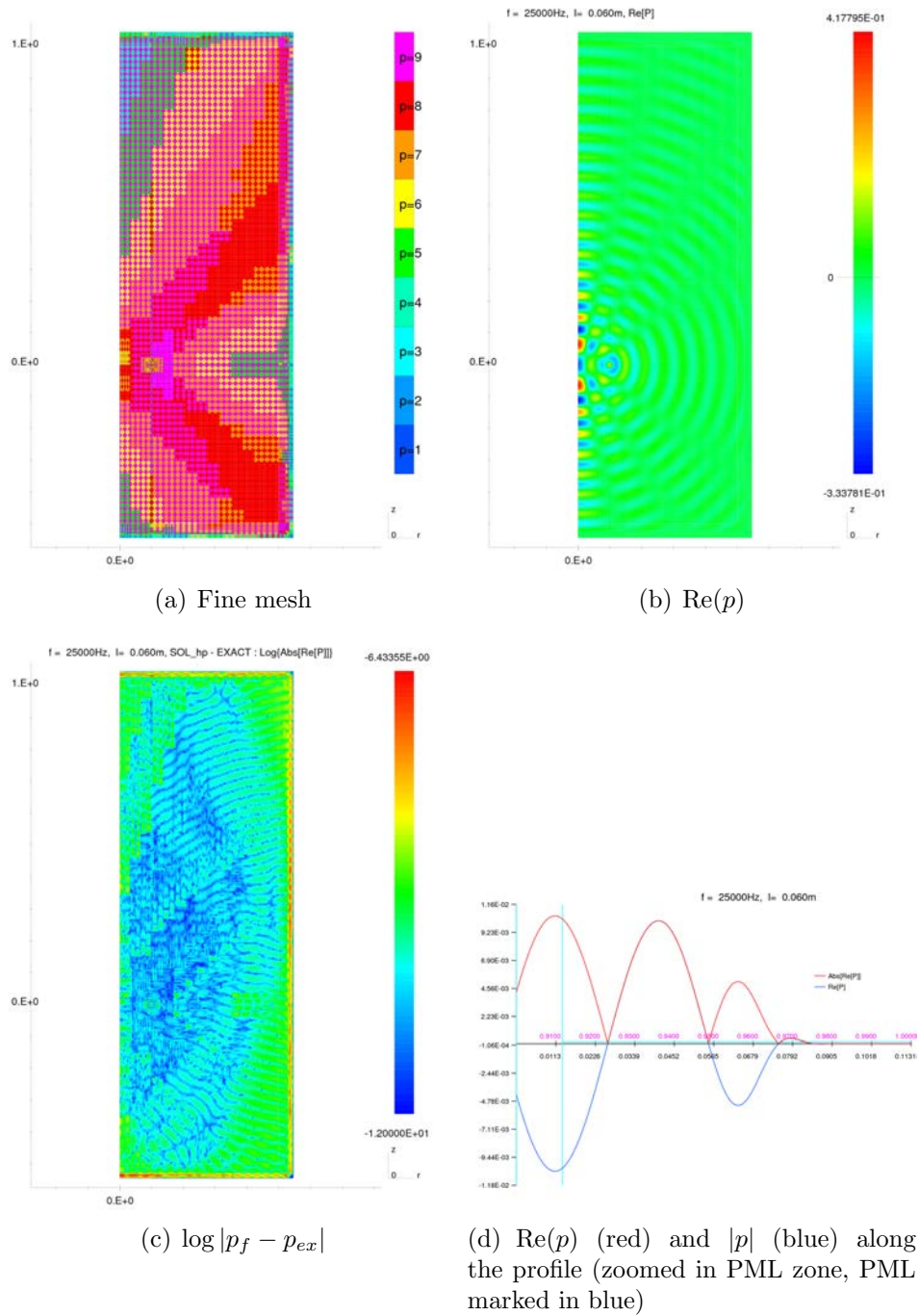Figure A.32: Acoustics. Ring source. Formulation A. $f = 50$ Hz

53

(a) Fine mesh

(b) Re(p)

(c) $\log |p_f - p_{ex}|$

(d) Re(p) (red) and $|p|$ (blue) along the profile (zoomed in PML zone, PML marked in blue)

Figure A.33: Acoustics. Ring source. Formulation A. $f = 25$ kHz

54

(a) Fine mesh

(b) Re(p)

(c) $\log|p_f - p_{ex}|$

(d) Re(p) (red) and $|p|$ (blue) along the profile (zoomed in PML zone, PML marked in blue)
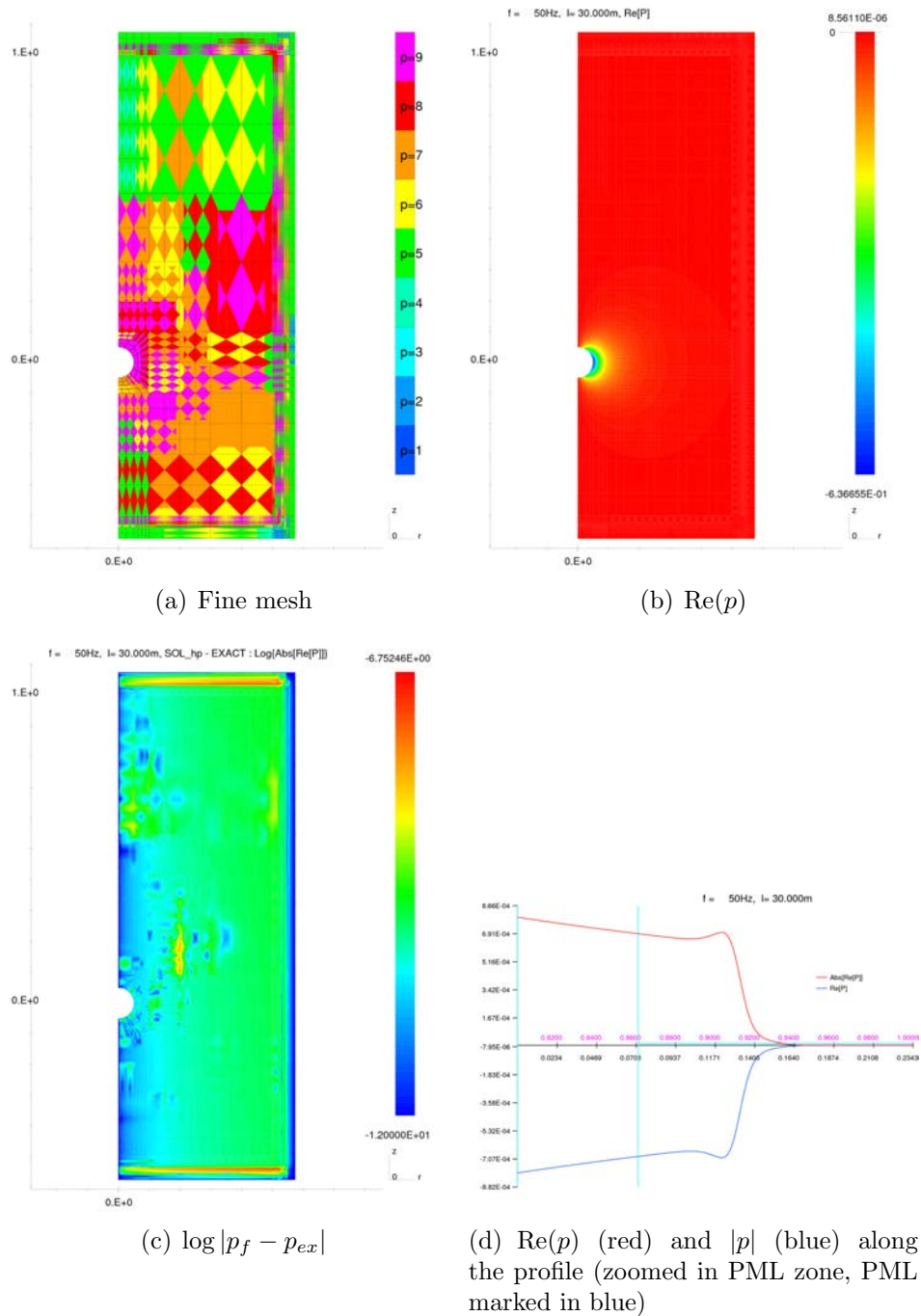
Figure A.34: Acoustics. Dipole point source. Formulation A. $f = 50$ Hz

(a) Fine mesh

(b) Re(p)

(c) $\log |p_f - p_{ex}|$

(d) Re(p) (red) and $|p|$ (blue) along the profile (zoomed in PML zone, PML marked in blue)
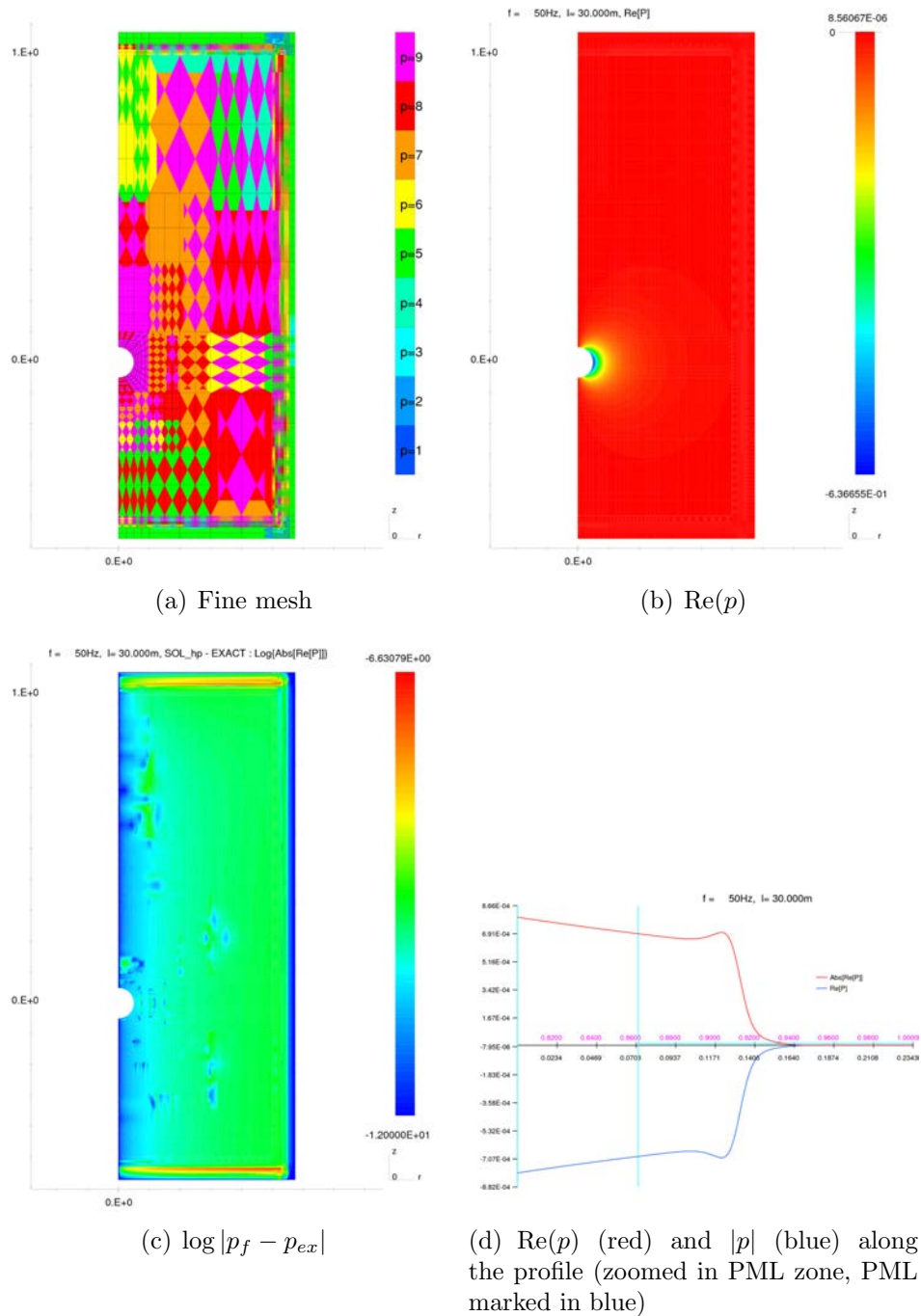
Figure A.35: Acoustics. Dipole point source. Formulation B. $f = 50$ Hz

(a) Fine mesh

(b) $\mathrm{Re}(p)$

(c) $\log |p_f - p_{ex}|$

(d) $\mathrm{Re}(p)$ (red) and $|p|$ (blue) along the profile (zoomed in PML zone, PML marked in blue)
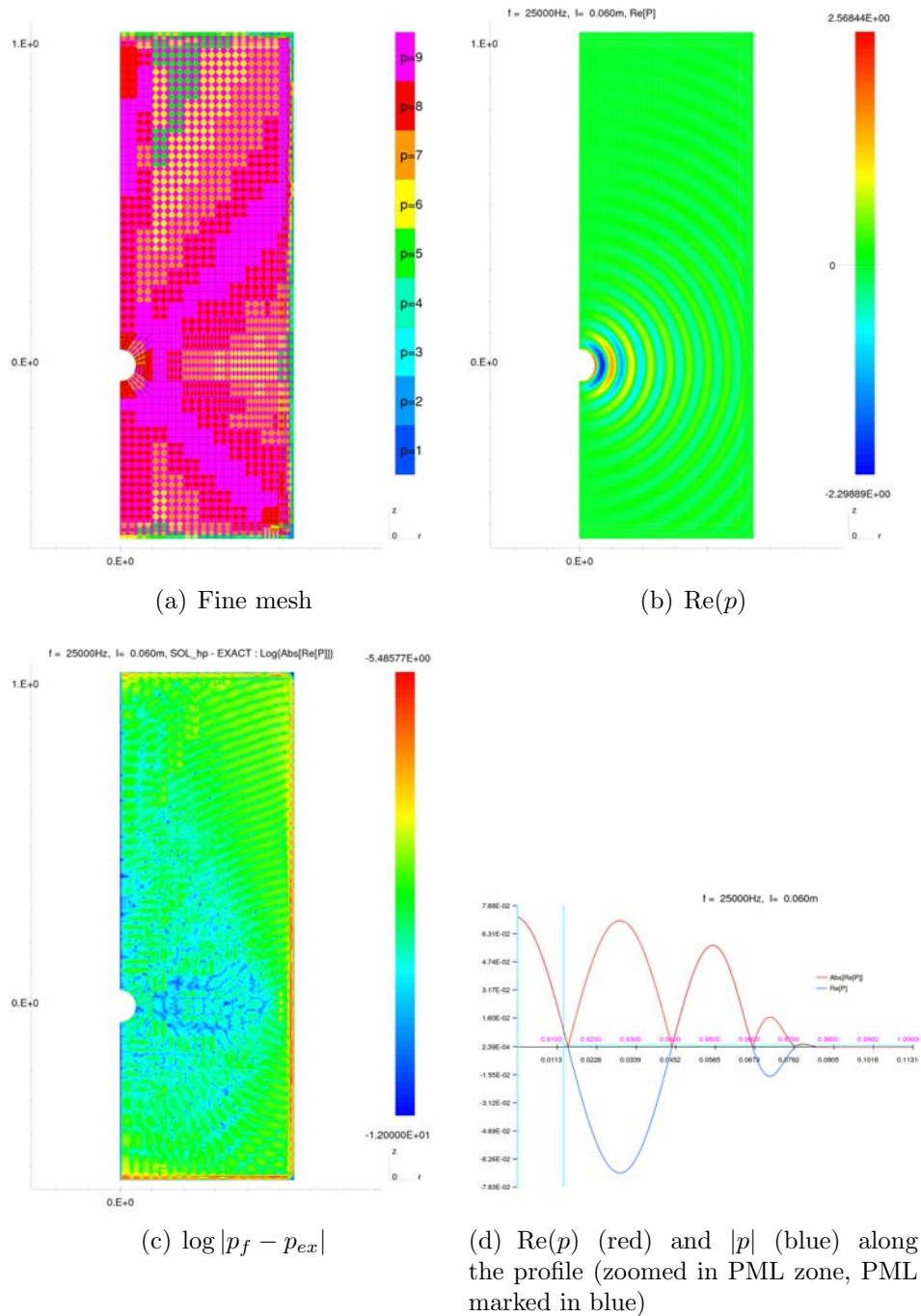
Figure A.36: Acoustics. Dipole point source. Formulation B. $f = 25$ kHz
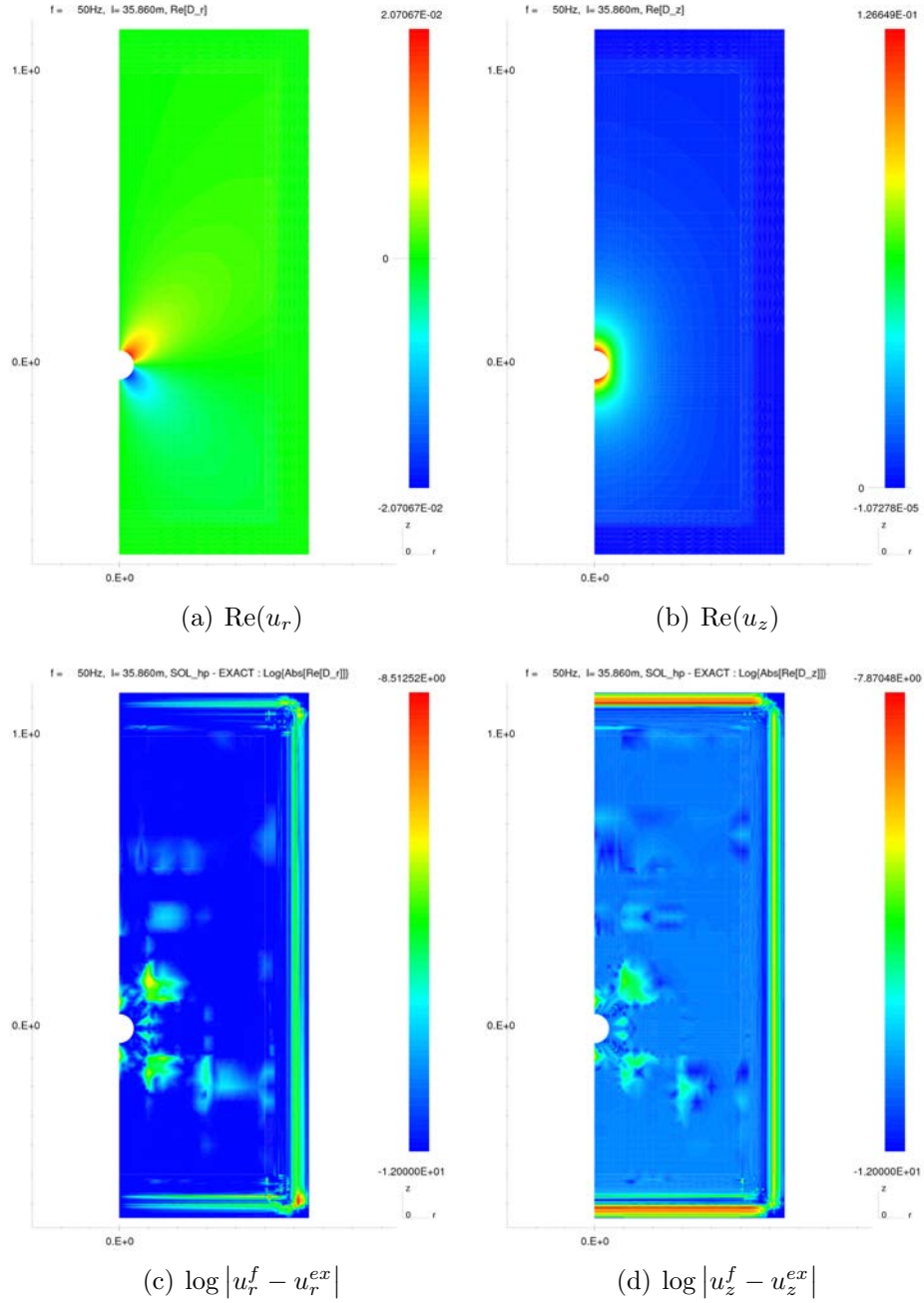
Appendix B. Verification of the elastic part of the code

(a) Re(u_r)

(b) Re(u_z)

(c) $\log \left| u_r^f - u_r^{ex} \right|$
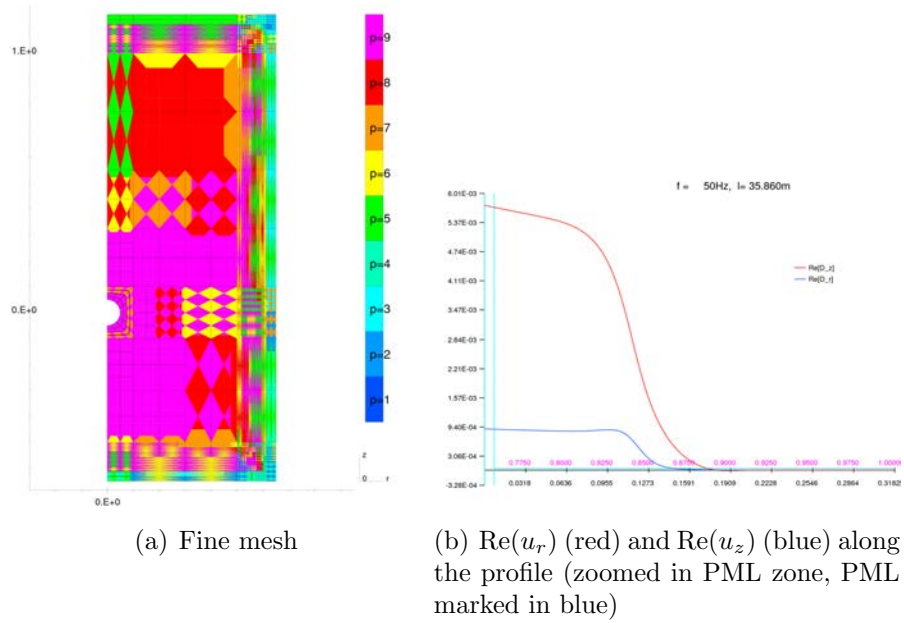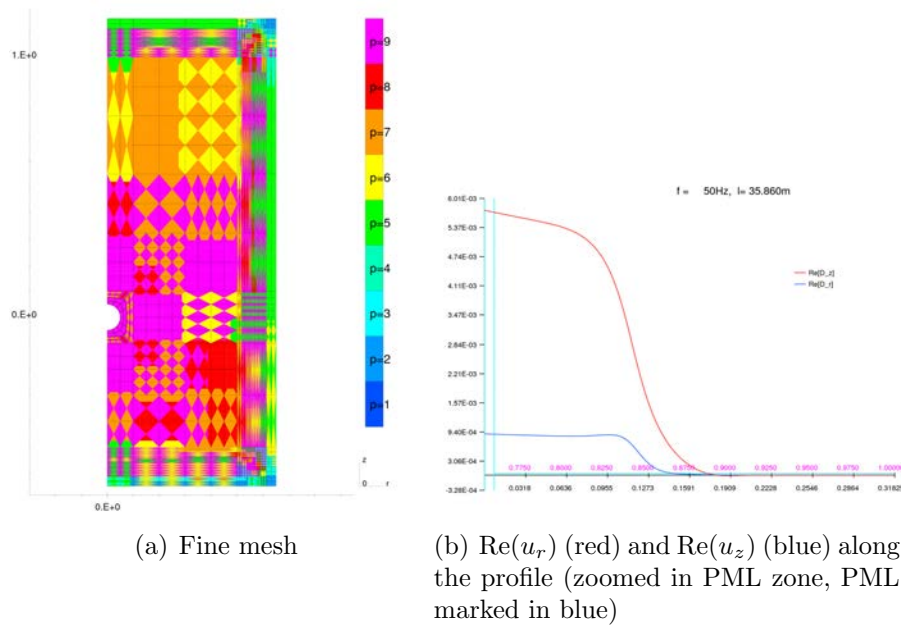

(d) $\log \left| u_z^f - u_z^{ex} \right|$

Figure B.37: Elasticity. Monopole point source. Formulation A. $f = 50Hz$

(a) Fine mesh

(b) $\mathrm{Re}(u_r)$ (red) and $\mathrm{Re}(u_z)$ (blue) along the profile (zoomed in PML zone, PML marked in blue)

Figure B.38: Elasticity. Monopole point source. Formulation A. $f = 50Hz$

(a) Fine mesh

(b) $\mathrm{Re}(u_r)$ (red) and $\mathrm{Re}(u_z)$ (blue) along the profile (zoomed in PML zone, PML marked in blue)
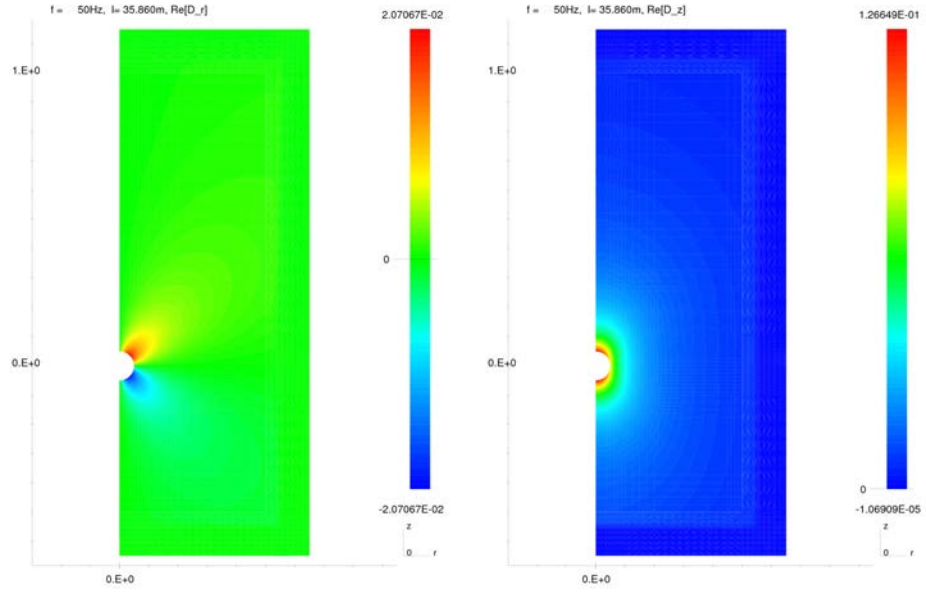
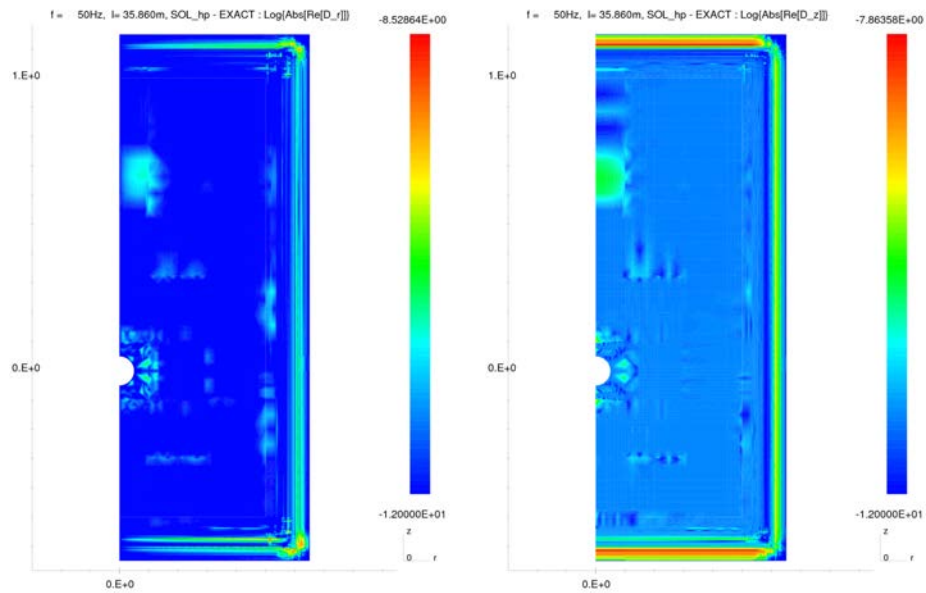Figure B.39: Elasticity. Monopole point source. Formulation B. $f = 50Hz$

60

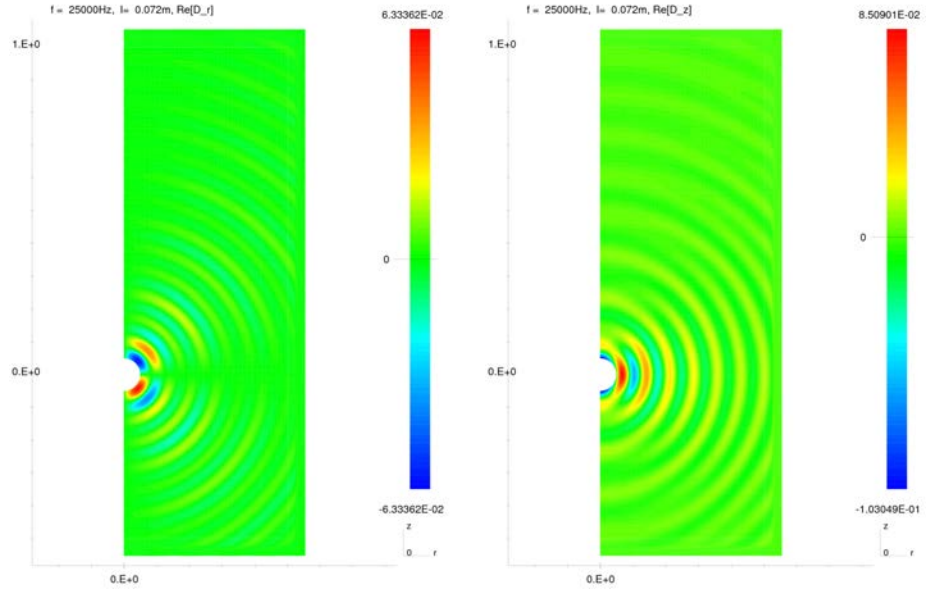(a) $\mathrm{Re}(u_r)$ (b) $\mathrm{Re}(u_z)$

(c) $\log\left|u_r^f - u_r^{ex}\right|$ (d) $\log\left|u_z^f - u_z^{ex}\right|$

Figure B.40: Elasticity. Monopole point source. Formulation B. $f = 50Hz$

61

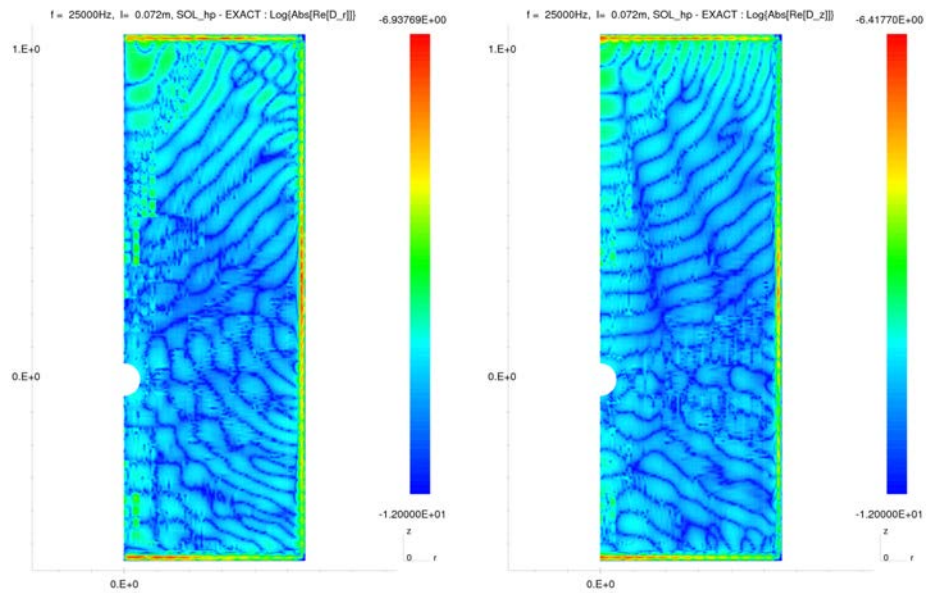(a) Re(u_r)

(b) Re(u_z)

(c) $\log \left| u_r^f - u_r^{ex} \right|$

(d) $\log \left| u_z^f - u_z^{ex} \right|$

Figure B.41: Elasticity. Monopole point source. Formulation A. $f = 25kHz$

(a) Fine mesh

(b) $\mathrm{Re}(u_r)$ (red) and $\mathrm{Re}(u_z)$ (blue) along the profile (zoomed in PML zone, PML marked in blue)

Figure B.42: Elasticity. Monopole point source. Formulation A. $f = 25kHz$

(a) Fine mesh

(b) $\mathrm{Re}(u_r)$ (red) and $\mathrm{Re}(u_z)$ (blue) along the profile (zoomed in PML zone, PML marked in blue)
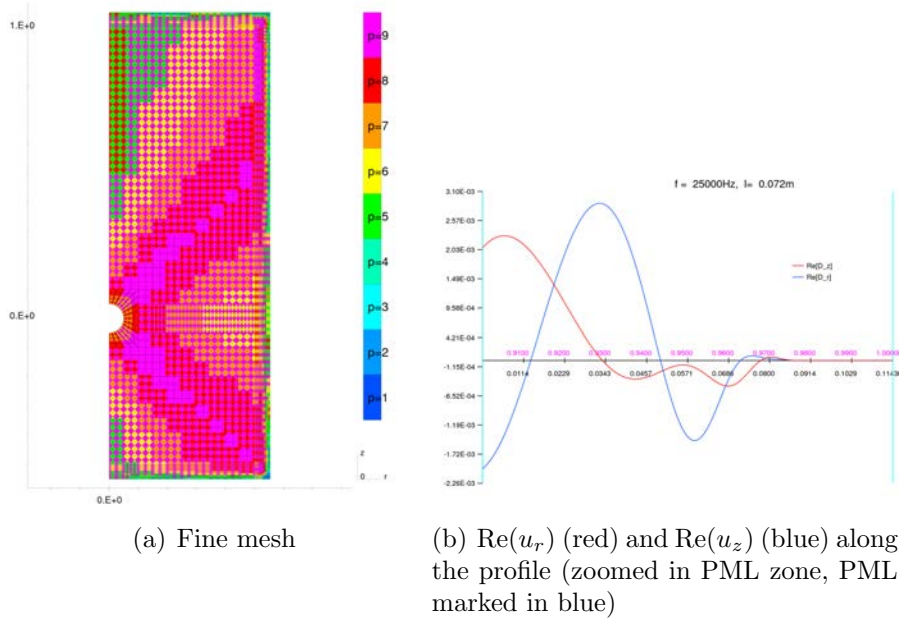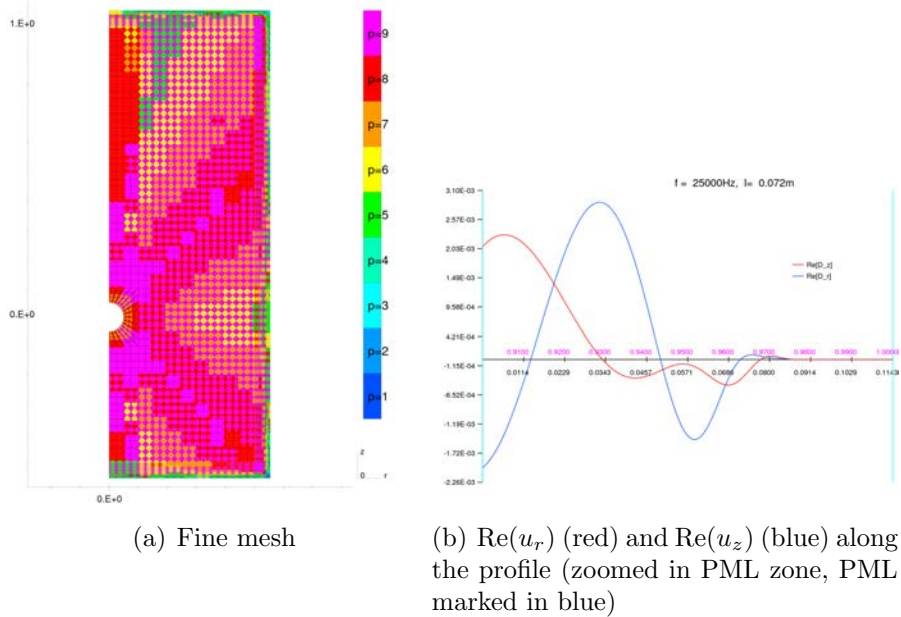
Figure B.43: Elasticity. Monopole point source. Formulation B. $f = 25kHz$

f = 25000Hz, l= 0.072m, Re[D_r]   6.33362E-02

(a) Re(u_r)

f = 25000Hz, l= 0.072m, Re[D_z]   8.50901E-02

(b) Re(u_z)

f = 25000Hz, l= 0.072m, SOL_hp - EXACT : Log{Abs[Re[D_r]]}   -6.56769E+00

(c) $\log \left| u_r^f - u_r^{ex} \right|$

f = 25000Hz, l= 0.072m, SOL_hp - EXACT : Log{Abs[Re[D_z]]}   -6.16595E+00
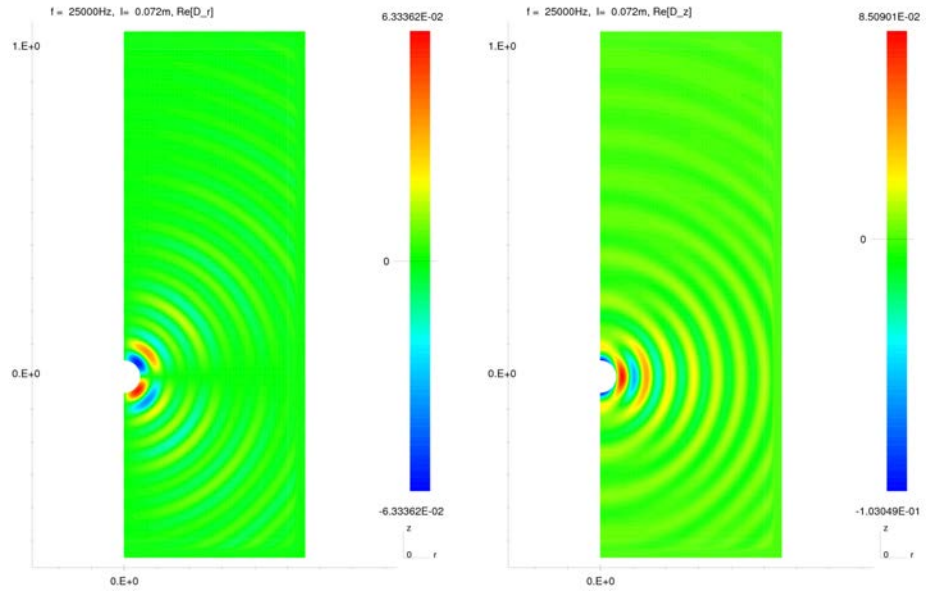
(d) $\log \left| u_z^f - u_z^{ex} \right|$

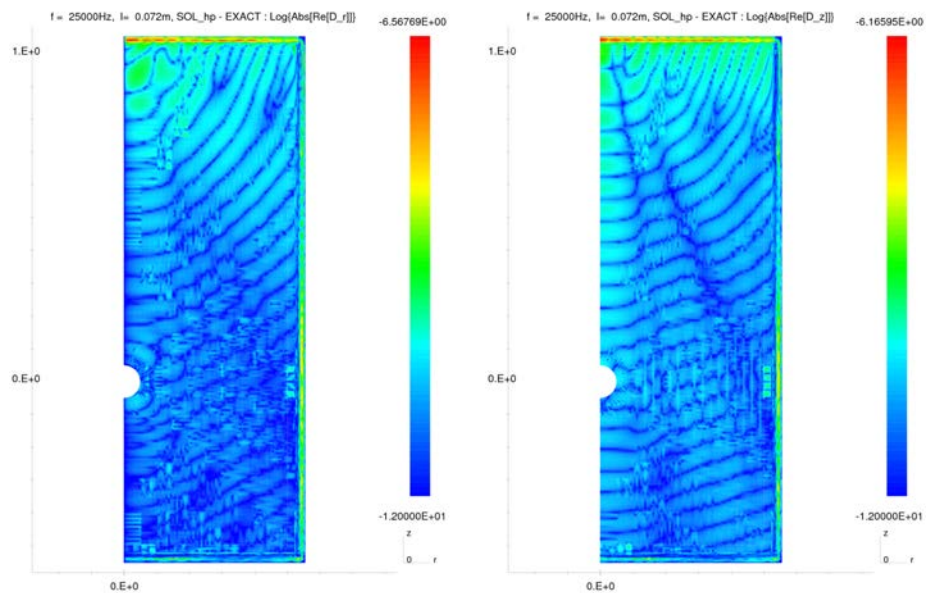Figure B.44: Elasticity. Monopole point source. Formulation B. $f = 25kHz$

64

(a) Re(u_r)

(b) Re(u_z)

(c) Re(u_θ)

(d) $\log \left| u_r^f - u_r^{ex} \right|$

(e) $\log \left| u_z^f - u_z^{ex} \right|$

(f) $\log \left| u_\theta^f - u_\theta^{ex} \right|$
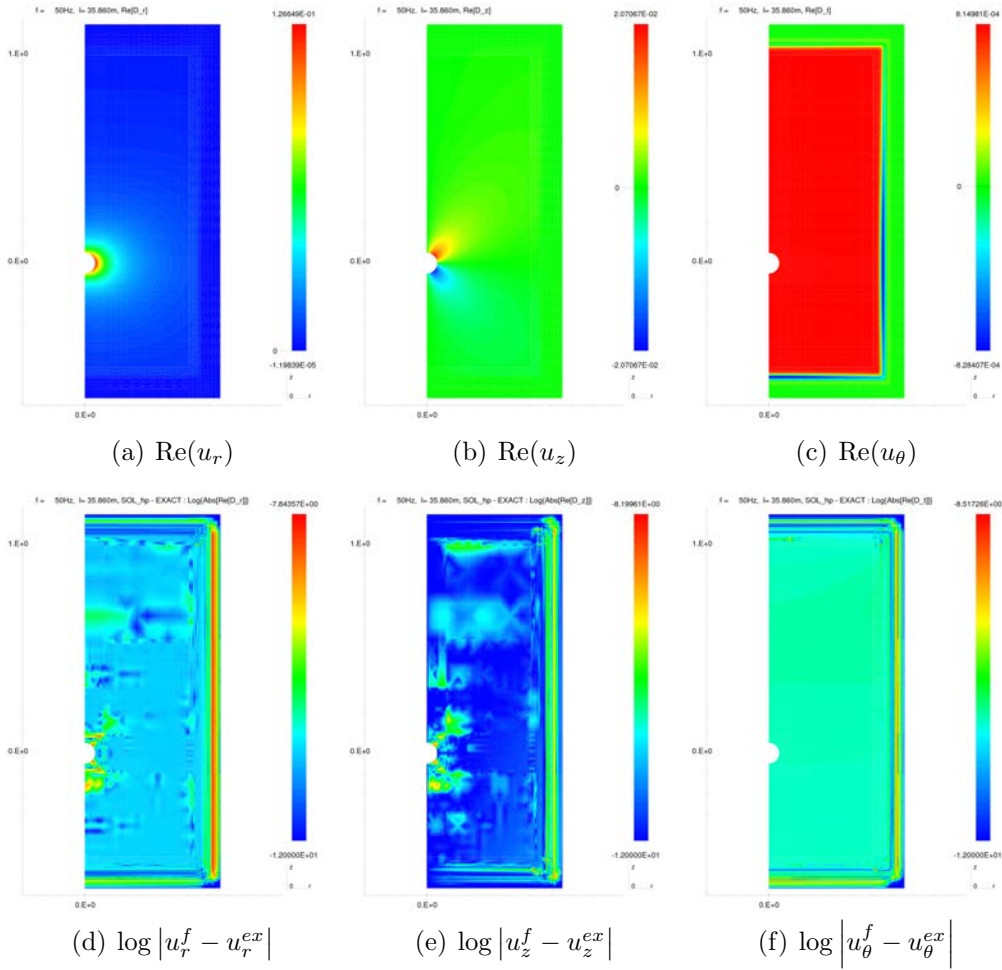
Figure B.45: Elasticity. Dipole point source. Formulation A. $f = 50Hz$

65

(a) Fine mesh

(b) Re(u_r), Re(u_z) and Re(u_theta) along the profile (zoomed in PML zone, PML marked in blue)
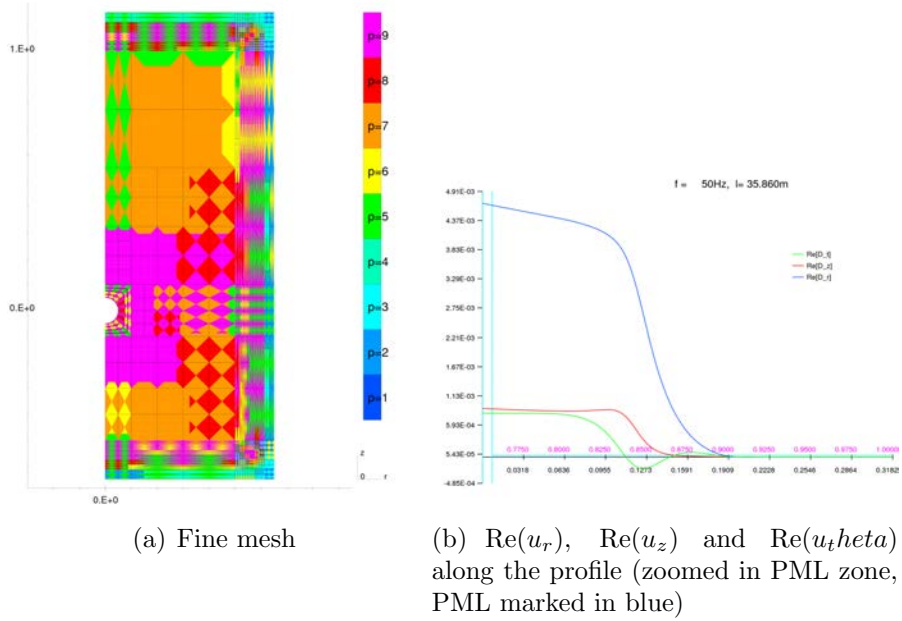
Figure B.46: Elasticity. Dipole point source. Formulation A. $f = 50Hz$

(a) Fine mesh

(b) Re(u_r), Re(u_z) and Re(u_theta) along the profile (zoomed in PML zone, PML marked in blue)
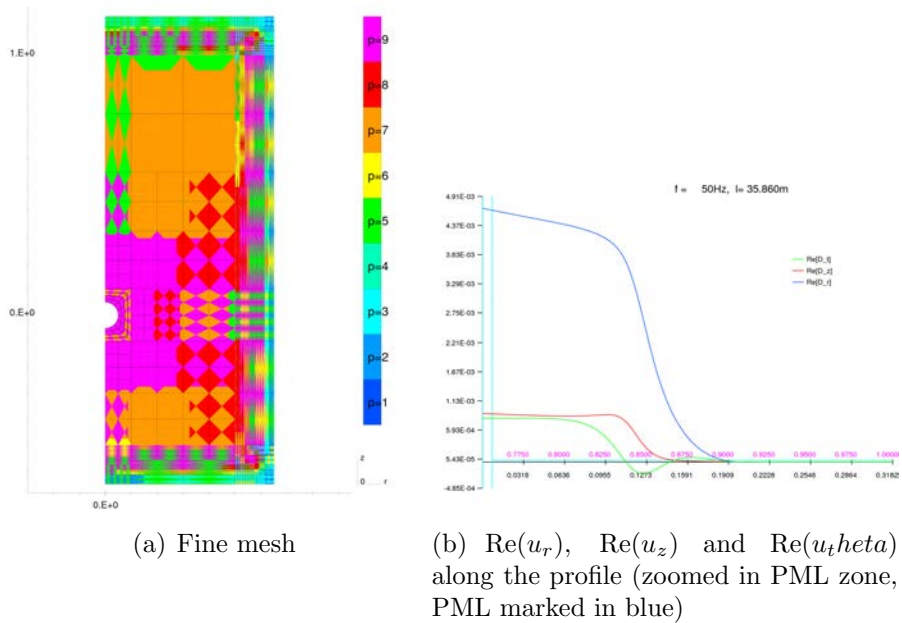
Figure B.47: Elasticity. Dipole point source. Formulation B. $f = 50Hz$

66

(a) Re(u_r)

(b) Re(u_z)

(c) Re(u_θ)

(d) $\log \left| u_r^f - u_r^{ex} \right|$

(e) $\log \left| u_z^f - u_z^{ex} \right|$

(f) $\log \left| u_\theta^f - u_\theta^{ex} \right|$
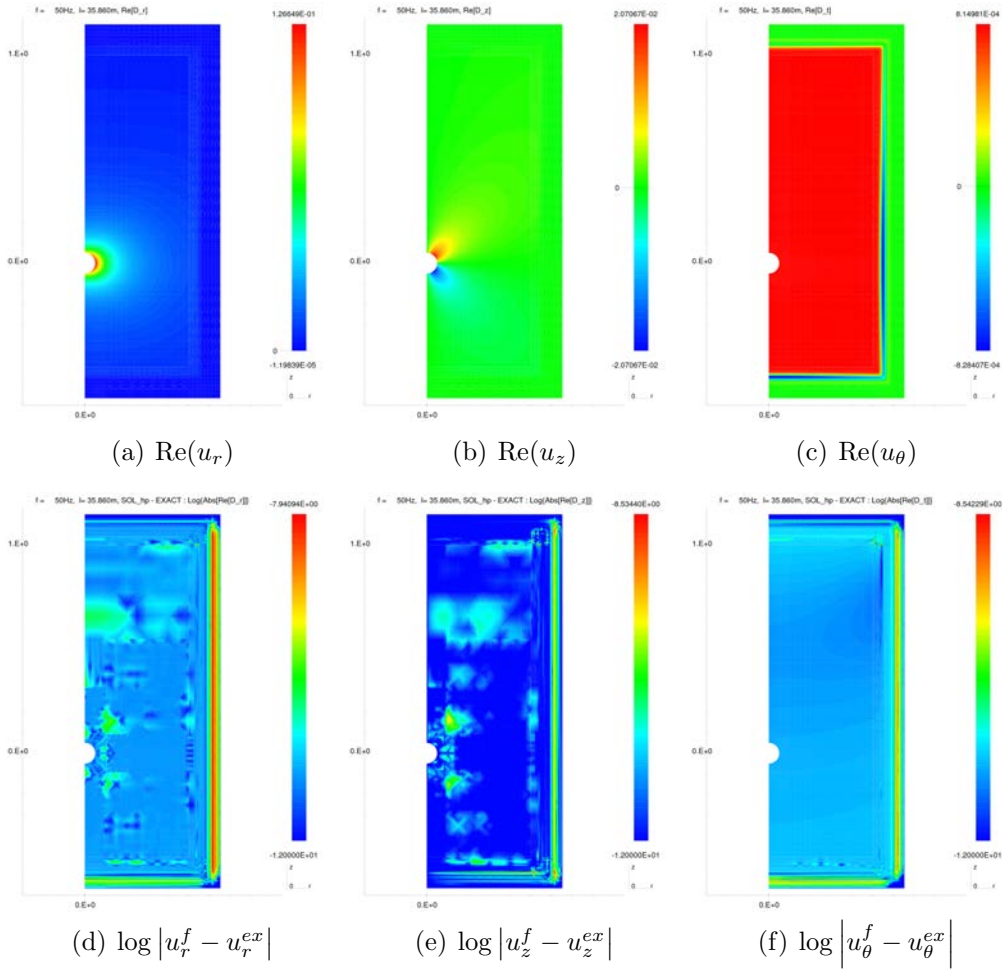
Figure B.48: Elasticity. Dipole point source. Formulation B. $f = 50Hz$

(a) Fine mesh

(b) $\mathrm{Re}(u_r)$, $\mathrm{Re}(u_z)$ and $\mathrm{Re}(u_theta)$ along the profile (zoomed in PML zone, PML marked in blue)
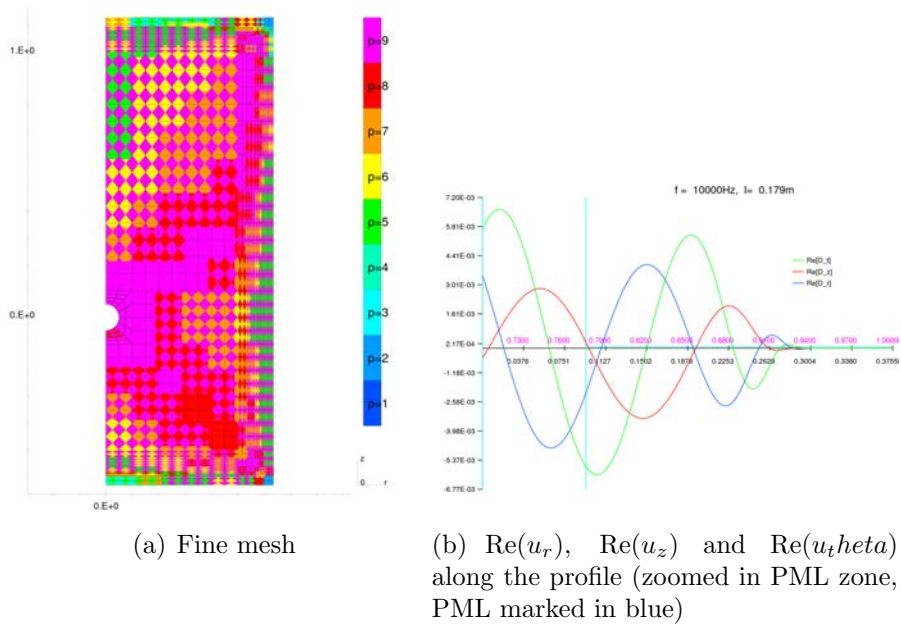
Figure B.49: Elasticity. Dipole point source. Formulation B. $f = 10kHz$

(a) $\mathrm{Re}(u_r)$

(b) $\mathrm{Re}(u_z)$

(c) $\mathrm{Re}(u_\theta)$

(d) $\log \left| u_r^f - u_r^{ex} \right|$

(e) $\log \left| u_z^f - u_z^{ex} \right|$
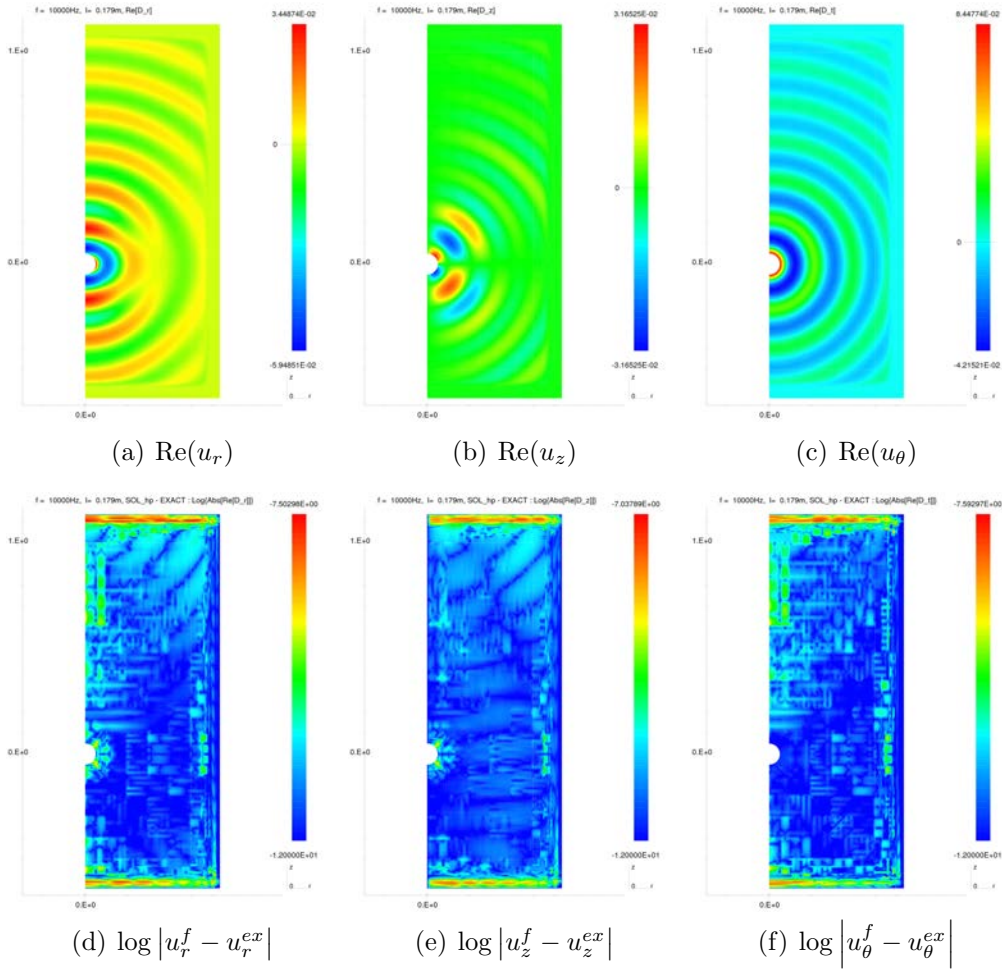
(f) $\log \left| u_\theta^f - u_\theta^{ex} \right|$

Figure B.50: Elasticity. Dipole point source. Formulation B. $f = 10kHz$

[1] C. Michler, L. Demkowicz, C. Torres-Verdin, Numerical simulation of borehole acoustic logging in the frequency and time domains with hp-adaptive finite elements, Comput. Methods Appl. Mech. Engrg. 198 (2009) 1821–1838.

[2] L. Demkowicz, Computing with hp Finite Elements. I.One- and Two-Dimensional Elliptic and Maxwell Problems, Chapman & Hall/CRC Press, Taylor and Francis, 2006.

[3] L. Demkowicz, J. Kurtz, D. Pardo, M. Paszyński, W. Rachowicz, A. Zdunek, Computing with hp Finite Elements. II. Frontiers: Three-Dimensional Elliptic and Maxwell Problems with Applications, Chapman & Hall/CRC, 2007.

[4] L. Demkowicz, J. Kurtz, An hp framework for coupled multiphysics problems, Tech. rep., ICES, in preparation (2010).

[5] H. Sanchez, E. Sanchez Palencia, Vibration and Coupling of Continuous Systems: Asymptotic Methods, Springer-Verlag, 1989.

[6] J. Oden, L. Demkowicz, Applied Functional Analysis for Science and Engineering, Chapman & Hall/CRC Press, Boca Raton, 2010, second edition.

[7] L. Demkowicz, Asymptotic convergence in finite and boundary element methods. Part 1: Theoretical results, Computers & Mathematics with Applications 27 (12) (1994) 69–84.

[8] L. Demkowicz, Asymptotic convergence in finite and boundary element methods. Part 2: The lbb constant for rigid and elastic problems, Computers & Mathematics with Applications 28 (6) (1994) 93–109.

[9] G. Gatica, A. Márquez, S. Meddahi, Analysis of the coupling of primal and dual-mixed finite element methods for a two-dimensional fluid – solid interaction problem, SIAM J. Numer. Anal. 45 (2007) 2072–2097.

[10] J. White, Underground Sound. Application of seismic waves., Vol. 18 of Methods in Geochemistry and Geophysics, Elsevier, 1983.

[11] F. L. Paillet, C. H. Cheng, Acoustic Waves in Boreholes, CRC Press, 1991.

[12] X.-M. Tang, A. Cheng, Quantitative Borehole Acoustic Methods, Vol. 24 of Handbook of Geophysical Exploration. Seismic Exploration., Elsevier, 2004.

[13] K. Bhasavanija, L. M. Nicoletis, T. K. Young, A finite difference model of an acoustic logging tool: the borehole in a horizontally layered gelogic medium, presented at the 52nd Ann. Mtg. and Expos. Soc. Explor. Geophys., , Dallas, 312–313 (1982).

[14] R. Stephen, F. Cardo-Casas, C. Cheng, Finite-difference synthetic acoustic logs, Geophysics 50 (10) (1985) 1588–1609.

[15] C. Randall, D. Scheibner, P. Wu, Multipole borehole acoustic waveforms: synthetic logs with beds and borehole washouts, Geophysics 56 (11) (1991) 1757–1769.

[16] H. Leslie, C. Randall, Multipole sources in boreholes penetrating anisotropic formations: Numerical and experimental results, J. Acoust. Soc. Amer. 91 (1) (1992) 12–27.

[17] N. Cheng, C. Cheng, M. Toksöz, Borehole wave propagation in three dimensions, J. Acoust. Soc. Amer. 97 (6) (1995) 3483–3493.

[18] T. Wang, X.-M. Tang, Finite-difference modeling of elastic wave propagation: a nonsplitting perfectly matched layer approach, Geophysics 68 (5) (2003) 1749–1755.

[19] B. Sinha, E. Şimşek, L. Q.-H., Elastic-wave propagation in deviated wells in anisotropic formations, Geophysics 71 (6) (2003) D191–D202.

[20] S. Chang, Finite element modeling of borehole acoustics, J. Acoust. Soc. Amer. 69 (S1) (1981) S90–S90.

[21] M. Frehner, S. M. Schmalholz, Finite-element simulations of stoneley guided-wave reflection and scattering at the tips of fluid-filled fractures, Geophysics 75(2) (2010) T23–T36.

[22] T. J. Chung, Applied Continuum Mechanics, Cambridge University Press, 1996.

[23] J. Pujol, Elastic Wave Propagation and Generation in Seismology, Cambridge University Press, 2003.

[24] K. Aki, P. G. Richards, Quantitative Seismology, University Science Books, 2002.

[25] G. A. Winbow, Compressional and shear arrivals in a multipole sonic log, Geophysics 50 (7) (1985) 1119–1126.

[26] J. H. Bramble, J. E. Pasciak, D. Trenev, Analysis of a finite PML approximation for the three dimensional elastic wave scattering problem, Mathematics of Computation (in press).

[27] M. Tezer-Sesgin, S. Dost, On the fundamental solutions of the axisymmetric Helmholtz-type equations, Applied Mathematical Modelling 17 (1993) 47–51.

[28] A. Ben-Menahem, S. J. Singh, Seismic Waves and Sources, Springer-Verlag, 1981.

[29] J. Ma, C. Torres-Verdin, Radial 1D simulation of multipole sonic waveforms in the presence of a centered non-rigid cylindrical tool and transversely isotropic elastic formations, in: C. Torres-Verdin (Ed.), 8th Annual Formation Evaluation Research Consortium Report, Center for Petroleum and Geosystems Enigineering. The University of Texas at Austin, 2008.

[30] E. Becache, S. Fauqueux, P. Joly, Stability of perfectly matched layers, group velocities and anisotropic waves, Journal of Computational Physics 188 (2003) 399–433.